Microchannel Flow Fields for Polymer Electrolyte Fuel Cells

Submitted as a partial requirement for the degree of Master of Science in Chemical Engineering

by

Tapiwa Chivengwa

May 2015

Supervisor:

Mr. Nabeel Hussain

PLAGIARISM DECLARATION

1. I know that plagiarism is wrong. Plagiarism is the use of another's work and to pretend that it is one's own.
2. I have used the Havard-UCT referencing style for citation and referencing. Each significant contribution to, and quotation in, this dissertation from other people's work has been acknowledged through citation and reference.

Signature: Date:

ABSTRACT

Fuel cell technology represents an efficient and relatively quiet way of generating electricity. Among the various types of fuel cells, the polymer electrolyte fuel cell (PEFC) is the leading candidate for portable, automotive and more recently stationary applications. One of the key challenges affecting both the performance and durability of low temperature PEFCs is water management.

Various water management strategies in PEFCs have been employed to date ranging from manipulation of operating conditions, fuel cell component design and flow field design to name a few. The optimisation of the flow field design for water removal has primarily focused on the use of flow channels which are in the minichannel range. This study investigated the use of a microchannel flow field design (channel hydraulic diameters of less than or equal to 200 μm) for a low temperature PEFC. Specifically it focused on the effect of using a microchannel design on overall fuel cell performance, pressure drop and the cell voltage behaviour over time. In addition the effect of different operating conditions was also investigated. The overall aim was to develop a more comprehensive understanding of the use of a microchannel based flow field system with specific focus on water management.

Fuel cell testing of two different flow field designs, namely a microchannel design and a more conventional commercial minichannel design, was performed in a single cell set up. Two operating conditions, cathode flow rate and cell compression, were varied and the effect on overall fuel cell performance and limiting current was investigated. Several diagnostic measurements including polarization curve, high frequency resistance, electrochemical impedance spectroscopy, pressure drop co-efficient and cell voltage monitoring were conducted to understand the water management behaviour and trends in the two different aforementioned flow field designs.

The microchannel flow field design showed similar trends (polarization curve and limiting current) to the commercial minichannel design when the operating conditions were changed. The microchannel design was however found to be more sensitive to changes in the cathode flow rate indicating easier water removal with increased drag force. Despite being less sensitive to the cathode flow rate, the fuel cell with commercial flow field design showed a greater overall degree of flooding, indicating water build-up in a component other than the flow field. Pressure drop co-efficient measurements showed a significant decrease in the co-efficient with increasing cathode flow rate for the microchannel design whilst for the commercial design the decrease was relatively less and the co-

efficient was closer to unity. Cell voltage measurements showed more fluctuations (frequency and size) at all the conditions tested for the commercial flow field design compared to the microchannel design which once again pointed to a greater degree of flooding.

The combined analysis of all the results strongly suggest that for the conditions tested in this study, most of water build-up for the fuel cell using the microchannel flow field design was in the flow channels whilst for the fuel cell with the commercial minichannel design the water build-up was predominantly in the gas diffusion layer (GDL). This coupled with the fact that the commercial design shows a greater degree of flooding implies that water build-up in the GDL is a stronger contributor to mass transfer limitations than water build-up in the flow channels. It also means that whilst the microchannel design showed characteristics of flooding in the channels, the design significantly reduced flooding in the GDL.

This study has developed a better understanding of the operation of a fuel cell using a microchannel flow field design. Specifically knowledge of water build-up and flooding in a fuel cell using a microchannel flow field design has been gained. It is recommended that the water imaging experiments such as neutron imaging be conducted on a fuel cell using a microchannel flow field design to more comprehensively map out the water distribution during fuel cell operation.

ACKNOWLEDGEMENTS

"*The material of the universe is always material, whether or not it be cognizable by man and subject to his thoughts and inventions and uses; and as man progresses in the practical and experimental studies – he will discover that there are things of the material in nature which to him are being developed and made known, and few which years before he had no conception of their existence*." – *Helen Padgett*

"*If man only knew what nature really is, and its laws, they would realize how little they now know of nature. Generally, nature is that consciousness of things material which comes within their limited cognition. They do not know that the larger part of nature, if it can be separated, is beyond the things or conditions which they have knowledge of as being material of the universe.*" – *Francis Bacon*

First and foremost, is a deep sense of gratitude to God for creating the universe and all its laws which allow us to exist in the material and are transparent so that anyone can freely investigate these laws and add to the few that mankind has discovered.

I would also like to thank Dr Olaf Conrad, for the opportunity and trust in my ability to study for a Master of Science degree in Chemical Engineering. A special thanks to my supervisor, Mr Nabeel Hussain, for his invaluable mentorship, equipment training, project advice, friendship and support. Mr Nabeel Hussain's time, energy and efforts played a significant role in ensuring a seamless study and guidance during the write-up phase. I would also like to thank my supervisor for offering me an eight month employment contract prior to my study.

I would also like to thank members of HySA/Catalysis for the financial, academic and ethical support throughout my study. Thanks to Mr Shiro Tanaka for allowing me to use some of his fuel cell components for this study.

Lastly, I would like to thank my wife and sons for being considerate, tolerant and patient with me.

TABLE OF CONTENTS

LIST OF FIGURES

LIST OF TABLES

LIST OF SYMBOLS

Symbol	Description	Units
$A_{channel}$	Channel cross-sectional area	m^2
C_{dl}	Double layer capacitance	C
D_{bolt}	Nominal bolt diameter	m
D_h	Hydraulic or equivalent diameter	m
F	Faraday's Constant (≈96.49)	$kC\ mol^{-1}$
f	Channel wall friction factor	
$\sum K_L$	Flow resistance due to turns or changes in flow direction	
$\frac{L}{D_H}$	Channel length to channel hydraulic diameter ratio	
m_{H20}	Mass production rate of water at the cathode side	g/s
M_{H2O}	Molecular mass of water (≈18)	$gmol^{-1}$
N_{bolts}	Number of bolts	
$N_{channels}$	Number of channels	
ρ	Fluid mixture density	kgm^{-3}
P^{sat}	Saturation vapour pressure	bar
P^{vap}	Partial pressure of water vapour	bar
ΔP	Pressure drop	bar
$\bar{Q}$	Volumetric flow rate	m^3
$\bar{Q}_{Total}$,	Total volumetric flow rate	m^3
Ψ_{wf}	water flooding severity	
T	Gas temperature	K
v	Average velocity	ms^{-1}

ΔV_{wf}^{ave}	Average voltage drop	V
V_b	Baseline Voltage	V
V_{wf}^{i}	Downward voltage peak (i^{th})	V
E	Total voltage of fuel cell	V
E_o	Standard electrode voltage at 1 bar	V
R	Ideal gas constant (≈8.314)	J $mol^{-1}K^{-1}$
RH	Relative Humidity	%
R_s	Ohmic impedance	Ω
R_{ct}	Charge-transfer impedance	Ω
#	Moles of electrons per molecule of hydrogen	
λ	Gas molecule's free mean path	m
$wt\%$	Mass as a fraction of the total mass	%

NOMENCLATURE

AC	Alternating Current
AFC	Alkaline Fuel Cell (s)
Bara	Absolute pressure in bars
Barg	Gauge pressure in bars
CCM	Catalyst Coated Membrane (s)
DC	Direct Current
DMFC	Direct Methanol Fuel Cell
EIS	Electrochemical Impedance Spectroscopy
GDL	Gas Diffusion Layer
MCFC	Molten Carbonate Fuel Cell (s)
MEA	Membrane Electrode Assembly
MPL	Microporous layer
OCV	Open Circuit Voltage
PAFC	Phosphoric Acid Fuel Cell (s)
PEFC	Polymer Electrolyte Fuel Cell (s)
PTFE	Poly-tetrafluoroethylene
SOFC	Solid Oxide Fuel Cell (s)
UEA	Unitized Electrode Assembly
W	Warburg Impedance
WTP	Water Transport Plate

1. Introduction

Fuel cell technology represents an efficient and relatively quiet way of generating electricity. Among the various types of fuel cells, the polymer electrolyte fuel cell (PEFC) is the leading candidate for portable, automotive and more recently stationary applications (Li & Sabir, 2005). Two of the major challenges currently inhibiting the full scale commercialization of this technology is the cost, both materials and production, and durability (Li et al., 2008). Most research activities to reduce cost are related to the improving the performance and specifically the power density output of current technologies with the overall aim of reducing the total amount of materials required.

One of the key challenges affecting both the performance and durability of low temperature PEFCs is water management. Water is required for optimal functionality of the membrane, specifically to improve its proton conductivity. On the other hand, if the liquid water formed on the cathode side of the fuel cell is not removed quickly enough, it can build-up within the various components in the cathode compartment. The build-up of liquid water prevents the access of reactant gases to the catalyst layer leading to mass transfer limitations and a significant drop in overall performance (He, Lin & Nguyen, 2003). Water management is particularly important for automotive and portable fuel cell applications which require high power density fuel cell systems due to space limitations. High power densities are typically achieved by operating the fuel cell in the high current density region. In this region, the rate of water production is at a maximum and adequate water removal and water management is crucial to maintaining fuel cell performance and durability.

Various water management strategies have been employed to date (Qi & Kaufman, 2002; Park et al., 2004; Li et al., 2008; Fabian et al., 2010). These have ranged from manipulation of operating conditions, design of materials within the fuel cell with specific water behaviour properties, flow field design and more active strategies involving the use of external components or devices. The best choice of strategy typically depends on the final fuel cell application requirements. The optimisation of the flow field design for water removal has primarily focused on the use of flow channels which are in the minichannel range (hydraulic diameters of greater than 200 μm and less than 3 mm). Microchannels (less than or equal to 200 μm) have received less attention and offer potential advantages of reduced flooding within both the flow field and the gas diffusion layer (GDL), the component adjacent to the flow field. This study investigated the use of a microchannel flow field design for a low temperature PEFC. Specifically it aimed to develop a better understanding of the use of microchannel flow field design as a means of reducing water build-up in the cathode compartment of the fuel cell.

2. Literature Review

2.1 Fuel Cell Technology

2.1.1 Basic Structure and Operation

A fuel cell is an electrochemical device that directly converts chemical energy of a fuel and oxidant to electrical energy, water and heat. All fuel cells consist of a negative (anode), a positive (cathode) electrode, an electrolyte, an external circuit and a reactant delivery and exhaustion system (Edgerton, Germeshausen & Grier (EG & G) Technical Services, Inc., 2004).

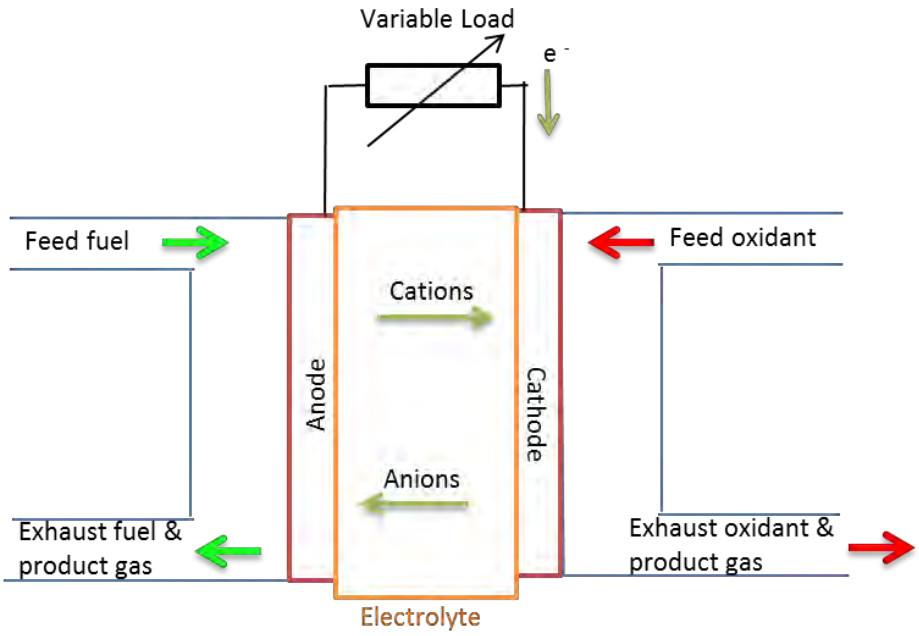

Figure 1: General Schematic of a Fuel Cell (EG & G Technical Services, Inc., 2004)

Reactants are fed to porous anode and cathode electrodes where corresponding half-cell reactions occur at the catalyst sites embedded in the electrodes. The potential difference as a result of the half-cell reactions provides a driving force for the electrons to flow between the electrodes resulting in the completion of a circuit (Serway & Jewett, 2014). At the same time, cations (or in some cases anions) are conveyed directly between the electrodes through a selective membrane or electrolyte. The main types of fuel cells are Alkaline Fuel Cells (AFCs), Molten Carbonate Fuel Cells (MCFCs), Phosphoric Acid Fuel Cells (PAFCs), Polymer Electrolyte Fuel Cells (PEFCs) and Solid Oxide Fuel Cells (SOFCs). Fuel cells are typically named after the type of electrolyte employed within their structures. The only exception is a special form of the PEFC that allows the direct use of methanol as a fuel and is labelled, Direct Methanol Fuel Cell (DMFC), after the fuel it uses (Carrette, Friedrich & Stimming, 2001).

2.1.2 Polymer Electrolyte Fuel Cells

PEFCs are the most attractive fuel cell type for automotive, stationary and portable applications (Marcinkoski, Kopasz & Benjamin, 2008). Perflourosulfonated acid polymers, supplied by Du Pont, Dow Chemical Company and Asahi Chemical Company (Costamagna & Srinivasan, 2001a), are typically used as the electrolytes to provide conductive pathways for cations, in this case protons, to migrate from the anode side to cathode side. The electrolyte must also act as a physical barrier between the fuel and oxidant gases (Gubler & Scherer, 2010). Proton conduction can occur by the Grotthuss mechanism whereby protons hop between hydrogen bonded water molecules and hydronium ions as well as by vehicle mechanism viz. diffusion and migration of hydronium ions (Ueki & Watanabe, 2008). Proton conductivity of the electrolyte increases with water content. To keep the membrane sufficiently hydrated, humidified reactant gases are fed to each electrode. Operation is typically limited to 80^{o}C, which allows for relatively quick start-ups and rapid response to load changes (Barbir, 2005).

One of the main disadvantages of PEFCs is that the catalyst employed at both electrodes is the noble and costly platinum. The platinum catalyst helps overcome the activation energy barriers, by providing alternative reaction routes with less activation energy requirements, and results in enhanced reaction rates. Unfortunately, platinum significantly increases the overall PEFC cost (Basu, 2007). Another potential disadvantage is the requirement for very pure hydrogen. Hydrogen fuel is typically produced from reforming of fossil fuel sources such as coal and natural gas which results in the co-generation of undesirable carbon oxides. An alternative process for hydrogen production is to electrolyze water. However, given that this process requires electricity, it is typically a lot more expensive to produce hydrogen from water electrolysis than it is to synthesize steam reformed hydrogen (Zoulias et al., 2004).

A single PEFC typically consists of end plates, insulator plates, current collector plates, bipolar plates, gaskets, gas diffusion layers (GDLs) and a catalyst coated membrane (CCM). The bipolar plates and platinum catalysts are significant contributors to the overall cost of PEFCs (Jeong & Oh, 2002; Wind et al., 2002; Tsuchiya & Kobayashi, 2004). Bipolar plates supply reactant gases to the GDLs via flow channels that are machined on a bipolar plate surface. The GDLs then distribute the fuel and oxidant gases uniformly over the anode and cathode catalyst layers, respectively, where the following half-cell reactions proceed at the platinum active sites;

$$H_2 \rightarrow 2H^+ + 2e^- \qquad \textbf{Equation 1}$$

$$2H^+ + \tfrac{1}{2}O_2 + 2e^- \rightarrow H_2O + heat \qquad \textbf{Equation 2}$$

Hydrogen is oxidized at the anode while oxygen is reduced at the cathode. The electrons released at the anode are driven to the cathode via an external circuit. The formation of water is a driving force for the reaction since the water is a low energy product from the exothermic reaction. The rate of water production, m_{H2O}, at the cathode per unit ampere of current generated is approximately 93.3 µg/s.

$$m_{H2O} = \frac{M_{H2O} I}{\#F} \qquad \textbf{Equation 3}$$

2.2 Bipolar plates

In a fuel cell stack, bipolar plates are located between the GDLs and current collector plates. According to the tenth edition of The Concise Oxford Dictionary (1999), the term bipolar is used to describe a device that is related to both positive and negative terminals of a magnetic or electric field. Bipolar plates have channels on both sides of a conductive and gas impermeable material to distribute fuel and oxidant gases to the anode and cathode of two adjacent cells, respectively (Barbir, 2005). Within a single cell configuration, channels are only on one side of each bipolar plate. The roles of bipolar plates in a single cell set-up are to (Larminie & Dicks, 2003);

- conduct electrons from the GDL to current collector plate at the anode side
- conduct electrons from the current collector plate to GDL at the cathode side
- provide structural support for the thin CCM and brittle GDLs
- provide a medium to remove the heat released at the cathode side CCM
- house the flow field channels to distribute reactant gases towards the GDLs
- allow the exhaustion of liquid water from the PEFC via the flow field channels

Since bipolar plates are multifunctional, multiple names are interchangeably used such as separator plates (Li & Sabir, 2005), flow-field plates, monopolar plates (Hamilton & Pollet, 2010) or halves of a bipolar plate (Barbir, 2005). In order to meet the bipolar plate functional requirements, the choice of bipolar plate material must be highly conductive (both electrically and thermally), corrosion resistant under acidic fuel cell operation conditions, mechanically strong yet light weighted and impermeable to the reactant gases (Li & Sabir, 2005). Mehta and Cooper (2003) recommended that the choice of bipolar material must have the following properties;

- a plate resistance of less than 0.01 Ω cm^2 for high electrical conductivity
- a corrosion rate of less than 0.016 mA/cm^2
- a compressive strength greater than 0.15 MPa
- a gas permeability of less than 1.0 x 10^{-4} $cm^3/s\ cm^2$
- a material and fabrication cost of less than US$ 0.0045 per cm^{-2}
- a density of less than 5 g/cm^3.

Bipolar plates contribute a significant portion of the PEFCs volume, weight and cost. The US DOE (2011) set a subprogram for the fuel cell research and development (R & D) community, to enable the fuel cell system's performance and cost competiveness for multiple applications. A cost target of US$30 per kilowatt and durability target of 5 000 hours were set for the automotive fuel cell system while a cost target of US$ 1 500 per kilowatt and durability target of 80 000 hours was set for stationary application systems in order to compete with other energy conversion devices.

The bipolar plate materials and manufacturing processes are the main reasons why bipolar plates are expensive (Spiegel, 2008). The most common materials are graphite, graphite composites and stainless steel. The manufacturing processes depend on the bipolar material used. Different materials have different advantages and disadvantages. Graphite is chemically stable and resistant to corrosion in the acidic environment of an operational PEFC but graphite is brittle and requires an expensive automated machining process to create flow channels on its surface (Hentall et al, 1999). Alternatively, composite graphite bipolar plates which consist of a combination of porous graphite and conductive carbonaceous fillers such as polyethylene, polypropylene and poly(vinylidene fluoride), are used to improve on the graphite's durability under mechanical shock or vibration, in addition to the relative ease of manufacture, in comparison to pure graphite bipolar plates (Busick & Wilson, 1999). Graphite composites generally undergo manufacturing methods of compression or injection moulding (Rayment & Sherwin, 2003).

In comparison to metallic bipolar plates, graphite composite bipolar plates have a lower mechanical strength and a lower electrical conductivity (Choi et al., 2012). Metallic bipolar plates offer availability for lower mass production costs, better mechanical strength and conductivity than graphite based bipolar plates (Wang et al., 2009). However, when exposed to an acidic environment, as is the case in PEFC, the metallic material is susceptible to corrosion or dissolution. Corrosion can subsequently lead to the contamination of the polymer electrolyte and result in membrane poisoning (Taherian, 2014). Furthermore, corrosion leads to a passive oxide layer formation on the surface of the metal, resulting in a high ohmic resistance and undesirable voltage drops (Hermann, Chaudhuri & Spagnol, 2005; Karimi et al., 2012). In order to prevent corrosion, metallic bipolar plates

must be coated with any of a conductive polymer, diamond-like carbon, noble metal, metal nitride, metal carbide or an oxide (Barbir, 2005). Wind et al. (2002) showed that the lifetime performance curve measured over a 1 000 hour period from a PEFC with gold coated stainless steel (316L) was identical to that obtained when graphite bipolar plates were used.

2.2.1 Flow Fields

The flow field patterns designed on the bipolar plates consist of land and channel areas. In an assembled cell, the land area compresses onto adjacent GDL areas while the channel areas remain open to corresponding GDL areas to allow gas and liquid phases to flow through the GDL and channel width interface. Careful design of the flow field pattern is necessary to ensure maximum reactant partial pressures in the electrode or catalyst layer, especially at high rates of reaction corresponding to high currents (Li & Sabir, 2005). The flow field channels are used to supply and distribute fuel and oxidant to the anode and cathode catalyst layers via GDLs, respectively.

Although parameters such as GDL thickness and the catalyst layer microstructure can be optimized to maximize reactant partial pressures, careful flow field design can also be effectively used to enhance the hydrogen and oxygen partial pressures at the respective catalyst sites (Nguyen, 2006). The flow field channels work to evenly distribute hydrogen and oxygen gases towards the catalyst layer and facilitate liquid water removal to keep mass transport losses to a minimum (Basu, 2007). The land areas are necessary to provide mechanical support for catalyst layer and GDL, in addition to an electrical pathway for the electrons between the bipolar plates and GDLs (Manso et al., 2012).

There is a need to optimize the flow field patterns because some of their functions present conflicts. For instance, while it is desirable for the flow field channels to allow uniform gas flow through the GDL towards the catalyst layers, electrical contact between the GDL and bipolar plate is simultaneously compromised at the channel areas (Vielstich, Lamm & Gasteiger, 2003). On the contrary, while the land areas offer electrical pathways as well as mechanical support for the GDLs and CCMs, broad land areas compromise the channel area for reactant gases and simultaneously promote water accumulation (Turhan et al., 2006; Hsieh & Chu, 2007). Based on the illustrated counteractive factors, it is essential to design the flow field channel and land areas in such a fashion that would minimize electrical contact losses and water accumulation, yet simultaneously deliver ample reactant partial pressures towards the catalyst layers.

2.2.2 Flow Field Designs

The flow field design strongly influences the reactant gas distribution and water management in PEFCs. According to Spiegel (2008), flow field design does not only account for even reactant distribution through the GDLs to the catalyst layers, but must also minimize reactant pressure drop in order to reduce parasitic pump requirements.

The most commonly used flow field designs used to date include straight or parallel, interdigitated and single or multichannel serpentine (Nguyen, 1996; Williams, Kunz & Fenton, 2004; Li & Sabir, 2005; Shimpalee, Greenway & Van Zee, 2006; Turhan et al., 2006; Xu & Zhao, 2006; Yamada et al., 2006; Nam et al., 2009; Wang & Wang, 2012). Figure 2 illustrates the aforementioned designs.

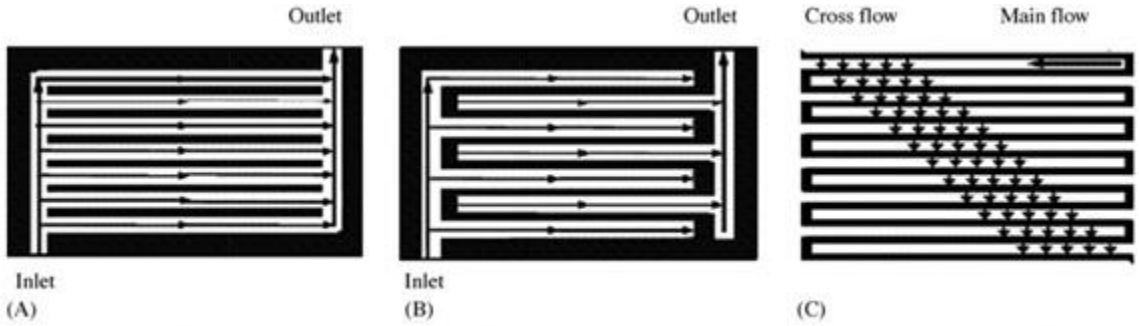

Figure 2: (A) Parallel, (B) Interdigitated, and (C) Single-Channel Serpentine flow field configurations (Li et al. (2008))

In the straight or parallel flow field configuration, the reactant gas flows within and along the channel areas. The channels are relatively short and have no directional changes and as a result the reactant gas experiences a smaller pressure drops than with other common configurations (Li & Sabir, 2005). The distribution of gas towards the catalyst layer, and vice versa, via the GDL occurs by diffusion. As a result, the rate of the electrochemical reactions within the catalyst layer can get limited by the reactant's rate of diffusion. This flow field design is suitable for applications in which high gas flow rates and low pressure drop are required (Nguyen, 2006).

Interdigitated flow field configurations are based on dead-end flow channel designs which forces the reactant gas to flow through the GDL by means of convective flow. Convective flow enhances an effective utilization of the catalyst layer through the facilitation of water removal in the land areas (Manso et al., 2012). Relatively high gas pressure is required since the reactant gas is forced to flow through the GDL instead of along the flow channels (Nguyen, 2006).

In a serpentine flow field configuration, the reactant gas flows along the continuous channel(s) and because of sufficient pressure drops between neighbouring channel sections, cross-flow or gas short circuit can occur through the GDL. Similarly to the convective flow effect in interdigitated flow field design, cross flow facilitates water removal from the land areas (Barbir, 2005). However, water settled in the channel corners may be difficult to push out, especially if channels are parallel to gravity (Owejan et al., 2007). The relatively long flow channels and numerous flow directional changes result in high pressure drop (Li et al., 2008).

The main difference among the three common flow field configurations is the pressure drop, ΔP, experienced by the reactants and degree of forced convection flow through the adjacent GDL in an assembled fuel cell. These differences strongly influence the reactant gas distribution and water management in the fuel cell.

According to Barbir (2005) ΔP through each flow field channel can be modelled as that of incompressible flow through pipes and conduits.

$$\Delta P = \left(\frac{\rho v^2}{2}\right)\left(f\left(\frac{L}{D_H}\right) + \sum K_L\right) \qquad \textbf{Equation 4}$$

As shown in Equation 4, the ΔP across the flow field channel is directly proportional to the average gas velocity, (v), and channel length, (L), and inversely proportional to the hydraulic or equivalent diameter, (D_H), of the channel. In addition, the pressure drop increases as the gas flow direction changes. The average gas velocity in a flow field channel is a function of the; total volumetric flow rate ($\bar{Q}_{Total}$), number of channels ($N_{channels}$) and channel cross-sectional area ($A_{channel}$), of each flow field design as illustrated below:

$$v = \frac{\bar{Q}_{Total}}{N_{channels} * A_{channel}} \qquad \textbf{Equation 5}$$

The average gas velocity is directly proportional to the total volumetric flow rate of reactant gas fed to the PEFC and inversely proportional to the flow field channel area.

2.2.3 Channel Shape and Dimensions

The channel shape and dimensions determine the channel's cross-sectional area and influence the average gas velocity in the flow channel. This in turn, as previously described, affects the ΔP in the channel. A variety of flow channel shapes such as circular, triangular, rectangular, hemispherical, parallelogram and trapezoidal have been illustrated, with the rectangular cross sectional shape being the most popular (Spiegel, 2008). The different flow channel shapes typically result from manufacturing processes rather than from functionality (Barbir, 2005).

Ahmed and Sung (2006) performed a three-dimensional simulation to investigate the effect of rectangular, trapezoidal and parallelogram shaped channel cross-sectional areas, of a straight flow field configuration, on water management at high operating current densities. The same channel cross-sectional area was maintained for all three shapes to ensure a constant average velocity in each case. The results of the simulation revealed that the rectangular shaped channel cross sectional area corresponded to higher cell voltages, whereas the trapezoidal shaped channel gave a more uniform reactant distribution, at a current density of 2.4 Acm^{-2}.

Owejan et al., (2007) used neutron radiography on triangular and rectangular shaped channels to obtain two-dimensional distributions of liquid water in an operational PEFC. The two different channel cross-sectional areas were kept the same and fashioned into a serpentine flow field configuration. It was found that the triangular shaped cross sectional channels retained less water than the rectangular shaped cross sectional channels. It was suggested that water tends to be transported in the corners of the channels while the gas flows in the high velocity core.

Typical channel dimensions are around 1 mm but may vary between 0.4 mm and 4 mm (Barbir, 2005). Channel dimensions refer to the channel width and depth. Kumar and Reddy (2003) studied the influence of channel dimensions in a single serpentine flow field design. The channel depth, width and land width were varied from 0.5 mm to 4 mm using Fluent® 6.0 and Gambit commercial software. With all permutations and combinations for varying the different dimension parameters viz. channel depth, width and land width, a total of 216 cases were numerically computed. It was found that the optimum channel depth, width and land width for the anode compartment was 1.5 mm, 1.5 mm and 0.5 mm respectively. A smaller land width arguably helps minimize water accumulation in the GDL than a wider land width. It is important to highlight that optimal dimensions might be dependent on neighbouring component properties, and therefore cannot be generalized for all combinations of individual PEFC component properties.

Variations in flow channel dimensions may occur due to machining tolerances and tool wear, which can cause deviance in flow field plates obtained from different suppliers (McCrabb et al., 2010). Shimpalee et al., (2011) used a computational continuum mechanics technique based on a commercial solver (STAR-CD 4.14) software, which had an add-on tool called expert system of PEFC version 2.5, to understand the effect of channel depth uniformity tolerances on pressure drop and overall PEFC performance. The simulation results showed that a larger deviation in channel depth, from the investigated average depth of 0.4 mm, gave a higher pressure drop. Moreover, it was found that shallower channels at the outlet gave higher pressure drop than shallower channels at

the inlet. In addition, it was found that the channel depth non-uniformity had minimal effect on the PEFC overall performance.

2.2.4 Microchannel Designs

Kandlikar and Grande (2002) proposed that flow channels that have a hydraulic diameter within the range of 10 – 200 μm, can be classified as microchannels. Table 1 summarizes the dimensional classifications suggested for microchannels, minichannels and conventional channels.

Table 1: Classification of Flow Channel Dimensions

Channel Category	Dimensional Range (μm)
Microchannel	$200 \geq D_h > 10$
Minichannel	$3000 \geq D_h > 200$
Conventional	$D_h > 3000$

The conventional manufacturing processes used in conventional PEFCs have restrictions on dimensions and scalability (Koç & Mahabunphachai, 2007). Microchannel patterns on PEFC metallic bipolar plates do not only provide compact mass and heat transfer benefits, but also affect the average gas velocity which directly controls the rate of convective mass and heat transport (Mahabunphachai & Koç, 2008). Kandlikar and Grande (2002) provided a comprehensive description of the fabrication processes for producing microchannels. The microchannel fabrication technology has pioneered the development of fuel cells in small dimensions and therefore facilitated the observation of scaling effects (Cha et al., 2004). Microfabrication technology involves a series of thin film material deposition and or removal (etch) steps that are used to create electrical or mechanical structures in and or on a substrate (Basu, 2007).

Cha et al (2004) employed photolithography techniques to prepare samples of channels with circular diameters of 5, 20, 100 μm and 500 μm. An optimum in the power density was found at a diameter of 100 μm. It was argued that the flooding area in the flow channels may be inversely proportional to diameter; meaning that the same amount of water would occupy more area in smaller diameters and increase the flooding severity. There must be an optimum diameter between 20 and 500 μm where convective mass transport is realized and water flooding is minimized. In addition to the experimental work, the researchers also utilized multiphysics fuel cell models in an attempt to verify these experimental findings. The modelling results suggested that the PEFC's power density would increase with decreasing diameter due to the reduced diffusion blockage of ribs and increased convective flow in microchannels. The conflict between the experimental and numerical work was

justified by the fact that latter work was only developed for a single phase flow, and not for two phase flow.

2.3 Effect of operating conditions on fuel cell performance

Operating parameters such as cathode flow rate (Larminie & Dicks, 2003; Hakenjos et al., 2004; Kim, Shimpalee & Van Zee, 2004; Barbir, 2005; Pasaogullari & Wang, 2005; Hussaini & Wang, 2009; Anderson et al., 2010; Zhang et al., 2010; Gerteisen et al., 2012), cell compression (Lee et al., 1999; Lee, Hsu & Huang, 2005; Zhou, Wu & Ma, 2007; Le Canut et al., 2009; Dotelli et al., 2011; Mason et al., 2012) and operating temperature and pressure (Zhang, Li & Zhang, 2009; Zhang et al., 2010) have a significant influence on PEFC performance and water transport characteristics. Several aspects of a fuel cell can be affected by the operating conditions such as reaction kinetics, membrane conductivity and mass transfer processes. In this study two operating conditions, namely cathode flow rate and cell compression are varied and are therefore reviewed in this section.

2.3.1 Cathode flow rate

The cathode flow rate or stoichiometry governs the total volume of oxidant entering the PEFC (Gerteisen et al., 2012) and affects the oxygen concentration or partial pressure in the catalyst layer (Larminie & Dicks, 2003; Barbir, 2005) and therefore the overall performance of the fuel cell. In general higher cathode flow rates lead to higher oxygen partial pressures in the flow channels and catalyst layer which in turn lead to improved performance (Gerteisen, Heilmann & Ziegler, 2009; Karimi et al., 2011). Increasing cathode flow rate also assists with the removal of liquid water in the flow channels (Barbir, 2005; Davey et al., 2008) by providing a greater force to push out the water. Kim, Shimpalee & Van Zee (2004) varied cathode stoichiometry in a triple serpentine flow field configuration. It was observed that an increase the cathode stoichiometric ratio from 2 to 3 significantly reduced the concentration polarization losses. However, it was noted that a more than double increase in stoichiometry at the anode side had negligible effect on the fuel cell overall performance.

Hussaini and Wang (2009) characterized liquid water removal from the GDL surface and gas channel qualitatively at different cathode flow rates. They used a transparent PEFC with gold coated stainless steel plates and seven straight chemically etched minichannels that each had approximate D_h of 667 µm with 1 mm wide lands between them. The in situ experiment and numerical study revealed that at sufficiently high gas flow rates, small droplets are swept away from the GDL surface by the gas flow thereby resulting in a mist flow pattern in the gas channel. It was also found that different flow patterns occurred under different gas flow rates. Although it is desirable to remove liquid water as quickly as possible to avoid water build-up from occurring, high flow rates result in higher parasitic

losses and reduce the efficiency of the overall PEFC system (Barbir, 2005; Pasaogullari & Wang, 2005).

Air is typically fed at a stoichiometric ratio of 2 or higher at the cathode side in order to prevent reactant starvation and water build-up from occurring (Larminie & Dicks, 2003; Barbir, 2005; Yousfi-Steiner et al., 2008). On the contrary, excess air compromises the overall PEFC efficiency and increases parasitic losses (Barbir, 2005; Pasaogullari & Wang, 2005). There is a need to optimize the reactant flow rate to prevent reactant starvation and flooding, while also minimizing parasitic losses.

Analytical models have been developed in an effort to determine the minimum air flow rate required to remove a single water droplet attached to the GDL surface. A force balance on the water droplet was proposed which included the drag and surface tension forces acting on the droplet (Kumbur, Sharp & Mench, 2006; Cho, Wang & Chen, 2012). The drag force was computed as a function of the air flow rate while the surface tension force was dependent on the GDL's hydrophobicity. Both analytical models highlighted the force balance must be dependent on other parameters such as operating conditions, flow channel cross-sections, position of droplet along flow channel, droplet diameter and droplet deformation behaviour. The complexity involved makes it challenging to theoretically determine the optimum air flow rate required to remove liquid water droplets from an operational PEFC.

Zhang et al. (2010) tested the effects of air flow rates on cell voltage fluctuations at a fixed current density of 0.5 A/cm^2 using a 50 cm^2 active area, triple serpentine flow field design with a D_h of 1000 µm, at 100% relative humidity (RH) and 80^{o}C. Cell voltage fluctuations were used as a measure of the extent of water build-up or flooding within the fuel cell. In order to quantitatively compare the severity of water flooding at different flow rates, a function, ψ_{wf}, was introduced. The symbol ψ_{wf} stands for the level of water flooding severity and is defined as a product of the number of voltage fluctuations caused by water flooding each minute, N_{wf}, and the average voltage drop, ΔV_{wf}^{ave}, caused by water flooding during the entire operating period. Each voltage drop is measured from a steady state voltage called the baseline voltage, V_b. Equations 6 & 7 illustrate how ψ_{wf} and ΔV_{wf}^{ave} were determined, respectively.

$$\psi_{wf} = N_{wf}\Delta V_{wf}^{ave} \qquad \textbf{Equation 6}$$

$$\Delta V_{wf}^{ave} = \frac{1}{n}\sum_{i=1}^{n}(V_b - V_{wf}^{i}) \qquad \textbf{Equation 7}$$

Water droplets can block the pores in the catalyst layer, GDL and gas flow channels and thereby hinder access of hydrogen and oxygen from flow channels to the catalyst sites. A rapid drop in cell voltage is often observed when the majority of pores are blocked. Furthermore, the blockages by water droplets in the flow channels result in a pressure drop increase in the flow channel. When this pressure differential reaches a threshold value, the water droplets are dragged out of the flow channels which may assist with less water build-up in the GDL pores and resulting in a swift voltage recovery. Figure 3 shows the typical voltage fluctuation plots obtained.

It was found that as the air stoichiometry increased from 2 to 3.5 at a current density of 0.5 A/cm^2, both the number of downward peaks and average voltage drop caused by water flooding decreased. It was confirmed that there is relatively less sufficient water removal at low air flow rates, and consequently water flooding severity is higher than at high air flow rates.

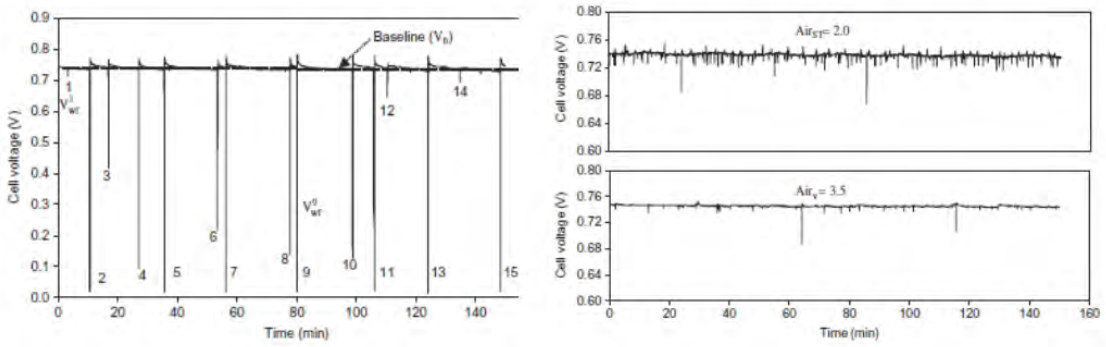

Figure 3: Voltage fluctuations as a function of time at different air flow rates. (Zhang et al., 2010)

Siefert and Litster (2011) reported experimental data on the mean voltage loss and fluctuations during constant current operation as a function of the air stoichiometric ratio. Straight flow field configurations and minichannels with hydraulic diameters of approximately 667 µm were used. The findings showed that for a fixed current density, the voltage losses and amplitude of fluctuations were inversely proportional to the air stoichiometric ratio.

In summary even though higher cathode flow rates and stoichiometries improve overall PEFC performance by reducing fuel cell flooding and mass transport losses, the use of high flow rates increases parasitic losses and reduce the overall efficiency of the PEFC system during operation (Pasaogullari & Wang, 2005).

2.3.2 Cell Compression

The catalyst layer, GDL, and bipolar plates need to be held together to minimise contact resistances for electron flow and to prevent leakage of gases from the fuel cell (Barbir, 2005). This is typically achieved by sandwiching the aforementioned individual components between two end plates, connected with several tie rods (Barbir, 2005; Spiegel, 2008). A clamping force is applied to hold the components in place and prevent loss of reactants to the environment. The clamping force is applied on one side of the PEFC through which it mechanically rotates bolts on tie-rods. The rotation of the bolts by the clamping force is often referred to as the clamping torque, τ, (Serway and Jewett, 2014).

For a given number of dry bolts, N_{bolts}, and bolt diameter, D_{bolt}, the following model can be used to approximate the relationship between clamping force and torque (Barbir, 2005):

$$Clamping\ Force = \frac{5N_{bolts}\tau}{D_{bolt}} \qquad \textbf{Equation 8}$$

The clamping force is directly proportional to both torque and the number of bolts, but inversely proportional to diameter of the bolts used.

The clamping pressure or compression pressure can be defined as the quotient of clamping force and the active area of the fuel cell. The clamping pressure affects the degree of compression of the catalyst layer and GDL, which in turn affects both liquid water and gas transport processes. (Ihonen et al., 2001). A clamping pressure range of 1.5 – 2.0 MPa is recommended to minimize the contact resistance between the GDLs and bipolar plates during operation (Barbir, 2005).

Lee et al. (1999) investigated the effect of different clamping forces on different GDLs in a 10 cm^2 serpentine flow field design. Three torques of 11, 14 and 17 Nm were applied on TORAY™, ELAT® and CARBEL® commercial GDLs. It was found that for ELAT® GDLs the overall performance with 14 Nm was better than that with 17 and 11 Nm. For the ELAT® GDLs, the overall performance with 17 Nm was better than that with 11 Nm. On the contrary, the TORAY™ GDLs gave best overall performance with 11 Nm instead of 14 or 17 Nm. It was also found that for a combination of TORAY™ and CARBEL® GDLs a sequence from 14 to 11 to 17 Nm was obtained in descending order from best overall performance. These findings indicated that the optimum compression pressure is different for different GDL materials.

Opu et al. (2010) investigated the effect of cell active area and clamping force on the overall performance of PEFCs. They found that increasing compression pressure decreased the interfacial contact resistance. Their results also showed that for the same cell compression pressure, the interfacial contact resistance for a smaller active area is less than that of a larger active area.

2.4 Water Management Strategies

One of the challenges for PEFC developers is the accumulation of liquid water in the fuel cell during operation. The liquid water build-up that results in a fuel cell performance drop is commonly referred to as flooding. Flooding increases the mass transfer resistance for reactant gases moving towards the catalyst layer and is mostly observed on the cathode compartment of the fuel cell (He, Lin & Nguyen, 2003). Flooding can occur in the flow channels, GDLs and catalyst layers of the fuel cell (Kandlikar, 2008).

According to Li et al. (2008), there exists a delicate balance between maintaining maximum membrane hydration and avoiding cathode side flooding. The desire to achieve this balance has driven a lot of researchers to developing flooding minimization water management strategies. Strategies developed to date can broadly be classified as modification of operation conditions, membrane electrode assembly (MEA) designs, flow field designs and active strategies involving the use of additional components (Nguyen, 2006). Some of the strategies have the undesirable effect of increasing the number of system components or parasitic load requirements thereby reducing the efficiency or increasing the size of the overall fuel cell system.

2.4.1 Operating conditions

Operating conditions as a strategy involves making changes to the operating conditions such as reactant gas flow rates, RH and cell compression. Changes to RH and cell compression to reduce flooding typically results in other negative effects on fuel cell performance such as increased membrane dehydration and increased contact resistance respectively. In addition, increasing the gas flow rate results in higher parasitic losses and compromises the overall system efficiency.

2.4.2 Membrane Electrode Assembly Design

The second strategy which has been employed is the modification of the internal fuel cell component properties, such as the electrolyte thickness and the microporous layer (MPL) and GDL wettability.

There are two mechanisms through which water is transported through the electrolyte membrane. The potential difference between the electrodes drives the protons generated at the anode to move, through the membrane, towards the cathode (Schmittinger & Vahidi, 2008). The protons move in the form of hydrated ions (Bagotsky, 2009) through a mechanism known as electro-osmotic drag (Basu, 2007). In addition to the electro-osmotic drag, water generated at the cathode results in a higher water concentration at the cathode than at the anode (Li et al., 2008). The concentration gradient is the driving force for the second mechanism known as back-diffusion, whereby water moves from the cathode to anode via the membrane (Spiegel, 2008).

Thinner membranes tend to promote back diffusion due to smaller diffusion distance (Barbir, 2005; Ge et al., 2005). This assists with removal of water from the cathode and can potentially reduce flooding (Wilkinson, Voss & Prater, 1994). However, thinner membranes experience a significantly higher gas cross-over rate and are less durable than thicker membranes since they are more prone to pin-hole formation (Basu, 2007).

Hydrophobic materials such as polytetrafluoroethylene, PTFE, are typically incorporated into the microporous layer (MPL) and GDL structures to assist with water expulsion. An MPL is typically used between the GDL and catalyst layer in order to improve the water management in this region (Kandlikar, 2008). Qi and Kaufman (2002) showed that the addition of an MPL between the GDL and catalyst layer enhanced the water management.

Incorporation of PTFE in the GDL structure results in hydrophobic and partially hydrophilic pores which remain free of liquid water and therefore prevent full water saturation of the GDL. Lin and Nguyen (2005) investigated the effect of GDL wettability on water management. They found that adding PTFE to the GDL enhanced gas and water transport when the fuel cell was operated under flooding conditions. Spernjak, Prasad and Advani (2007) used a transparent PEFC with a single serpentine flow field to observe how water behaved in PTFE treated and untreated GDLs. It was found that with treated GDLs water droplets emerged over the entire visible area while with untreated GDLs, water attached to the side walls and travelled along serpentine flow field channel mostly in the form of films and slugs. It was noted that the slugs were more difficult to remove than the water droplets.

Tüber, Pócza and Hebling (2003) also used a transparent PEFC to investigate water build-up in treated and untreated GDLs. They found that increasing the PTFE content decreased the surface tension of the GDL and made water removal easier than with untreated GDLs. Bevers, Rogers and von Bradke (1996) showed that there is a trade-off between the GDL's hydrophobicity and electrical conductivity. Their results showed that higher PTFE content lead to better hydrophobicity but poorer electrical conductivity. Lin and Nguyen (2005) did an extensive study on the effect of PTFE content on PEFC performance. It was found that addition of PTFE to the GDL could improve both gas and water transport, but an excessive PTFE loading (i.e.>40 wt %) could result in flooding within the catalyst layer.

By and large, fuel cell developers have extensively studied the effect of PTFE content on PEFC performance. The optimum amount depends on the operating conditions and operating current. In general, very high amounts of PTFE (i.e.>40 wt %) reduces electrical conductivity of the GDL and MPL and can reduce the number of hydrophilic pores in the layers to such an extent that it becomes difficult for water to travel from the cathode catalyst layer to flow channels. This in turn could result in catalyst layer flooding (Anderson et al., 2010).

2.4.3 Flow Field Design

The third approach that has been employed is the design of flow fields to ensure rapid water removal from the fuel cell. Appropriate design of flow channels over the active area has been considered to be the most successful strategy in addressing water flooding issues (Li et al., 2008). Flooding frequently occurs in the GDL, especially in the regions that are in direct contact with the flow field lands or ribs. In an effort to reduce the amount of water accumulation in the GDL, flow field patterns have been designed that result in pressure differentials between neighbouring channels to push out water trapped under the land. Flow field designs based on interdigitated or serpentine flow patterns are typically used to create pressure differentials (Nguyen, 1996).

The United Technologies Company (UTC) developed a water transport plate (WTP), which is a bipolar plate which has pores which are filled with liquid water (Yi, Yang & King, 2004). The WTPs have coolant flow channels that are continuously filled with water and gas flow channels that are in contact with the MEA or unitized electrode assembly (UEA) on both sides. Figure 4 shows a schematic of the WTP with two adjacent UEAs.

The WTP is gas impermeable but allows water to move from the gas flow channels to the coolant flow channels since gas streams are at a higher pressure than coolant streams (Anderson et al., 2010). As a result, water build-up in the flow channels is significantly reduced. In addition, applying a water concentration gradient can cause water to move from the coolant to gas flow channels, and thereby eliminate the need for external humidification (Yi, Yang and King, 2004).

The flow field can also be modified with respect to its hydrophobicity. Hydrophilic channels facilitate water transport in the walls of the channels (Quan & Lai, 2007). Cheah, Kevrekidis and Benziger. (2013) compared water formation and motion for square flow channels with hydrophilic and hydrophobic walls. It was found that the slugs formed in hydrophobic channels were smaller but greater in number than those formed in hydrophilic channels. A greater number of slugs was harder to remove and required more energy in the form of higher gas flow rates and therefore increased parasitic power requirements.

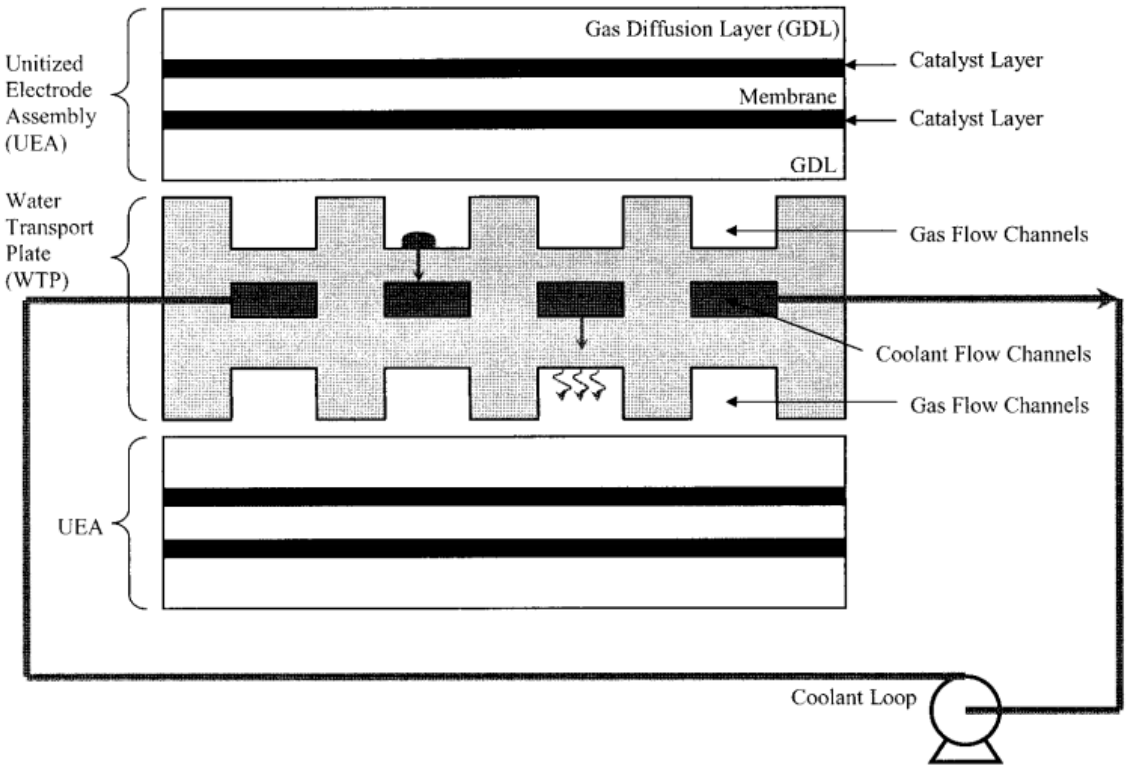

Figure 4: Schematic of the water transport plate. (Yi, Yang and King, 2004)

An alternative approach to reducing flooding involves reducing the land or rib width, which effectively reduces the area over which GDL flooding can occur. Cha et al., (2004) experimentally and numerically studied the overall performance of PEFCs with scaled down flow channel and rib widths. It was found that a more uniform reactant concentration was obtained in the GDL when the rib width was smaller than the GDL thickness. However, reducing the rib width without a corresponding reduction in channel width may compromise the contact area with the GDL and therefore contact resistance may increase (Barbir, 2005).

2.4.4 Active Strategies

Fuel cell developers have also looked into more, active low-power based water management approaches, such as the use of an electro-osmotic (EO) pump coupled with an electrically conductive wick. A wick is a porous material in which liquid water can be drawn by capillary action and is located between the flow field and EO pump (Fabian et al., 2010). EO pumps are devices that generate both flow and significant pressure capacity using electro-osmosis through channels (Yao & Santiago, 2003). Figure 5 shows a schematic of a flow field attached to a wick and EO pump.

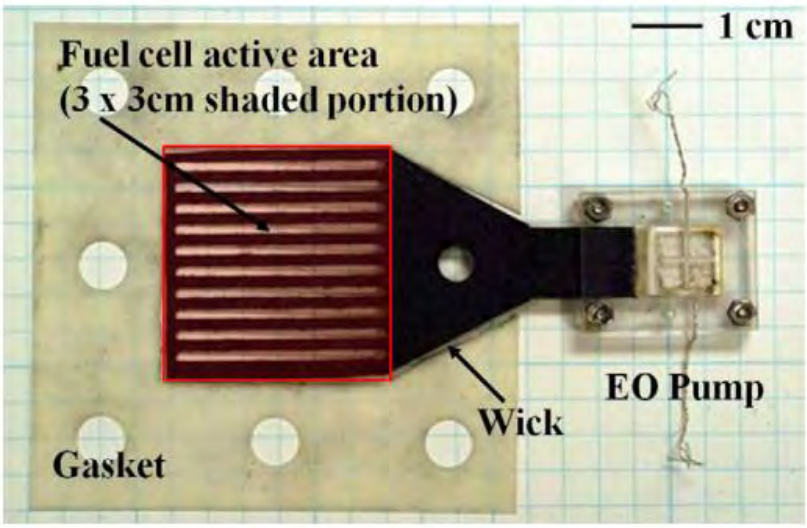

Figure 5: Schematic of an EO pump, wick and PEFC flow field. (Fabian et al., 2010)

The power supplied to the EO pump during operation is equivalent to about 1 % of the overall PEFC power at low current loads and approximately 0.5 % at medium to high current densities (Anderson et al., 2010).

Fabian et al. (2010) tested the overall performance of a PEFC with and without an EO pump and found that the cathode showed no signs of flooding when the EO pump was used. In addition, Fabian et al. (2010) performed steady state galvanostatic measurements with varying potential differences applied to the EO pump. It was found that less than 2 % of the PEFC's output power was required for the EO pump to fully stabilize the PEFC's voltage.

2.5 Characterization of fuel cell performance

This section presents an overview of the different in-situ electrochemical techniques that will be used in this study, namely polarization curve analysis and electrochemical impedance spectroscopy. A brief description of the use of pressure drop as a diagnostic tool is also presented.

2.5.1 Polarization Curves

The polarization curve is the most commonly used diagnostic tool to measure the overall performance of a single fuel cell or a fuel cell stack (Wu et al., 2008). The polarization curve is a plot of voltage against current density. Current density is the quotient of the current and active area and is typically used as it allows comparison between PEFCs of different sizes (Barbir, 2005). The polarization curve measurement is strongly dependant on fuel cell operating conditions (Spiegel, 2008). Figure 6 shows a typical polarization curve result. The final or actual polarization curve has three distinct regions in which specific losses dominate.

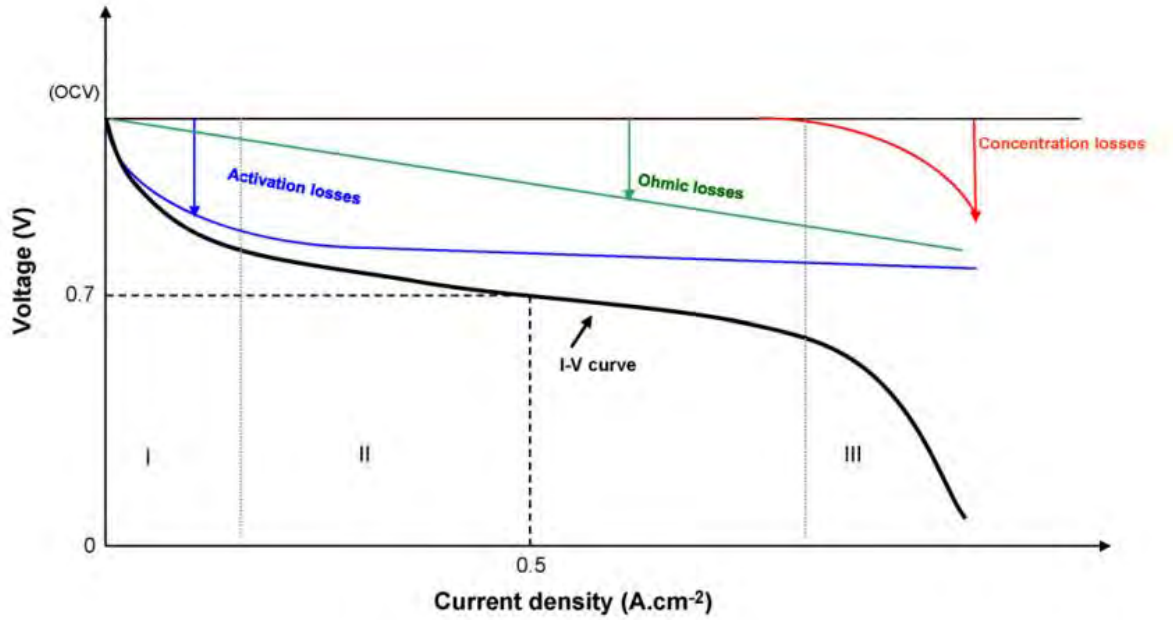

Figure 6: Schematic of a polarization curve (Yousfi-Steiner et al., 2008)

The three major voltage losses that dominate in regions I, II and III are activation, ohmic and concentration losses, respectively. The activation losses are associated with the slow kinetics of the oxygen reduction reaction and dominate at low current densities (Barbir, 2005). Ohmic losses consist of the resistance to proton flow through the membrane from anode to the cathode and resistance to electron flow through the different components of the fuel cell (Cooper et al., 2005). These losses dominate in the intermediate current density regions.

At higher current densities, concentration or mass transport losses dominate. This is due to a combination of (Barbir, 2005; Basu, 2007; Yousfi-Steiner et al., 2008):

- starvation of hydrogen and air at high reaction rates
- an inability of air to diffuse fast enough towards the cathode catalyst layer
- high rates of water production coupled with a slow water removal rate resulting in flooding

A limiting current density is typically used to characterize the mass controlled region at high current densities on a semi-log voltage vs. current plot (Cooper et al., 2005).

Whilst the polarization curve measurement provides a good indication of the fuel cell's overall performance and is a relatively quick and simple method, it does not completely isolate the different fuel cell performance losses and additional techniques are required to better understand the fuel cell performance (Wu et al., 2008).

2.5.2 Electrochemical Impedance Spectroscopy

Several of the processes that occur within a PEFC during operation such as mass-transfer (Barbir, 2005), electron flow and charge-transfer (Cooper et al., 2005) during the reaction are time or frequency dependent. Electrochemical impedance spectroscopy (EIS) is a technique that utilizes the frequency dependency of these processes to provide useful information on the different fuel cell performances losses (Wu et al., 2008). EIS is a relatively faster diagnostic tool than polarization curves but is significantly more complex to conduct and interpret.

In this technique, EIS, an alternating current (AC) signal of known amplitude and frequency is applied to the PEFC's direct current (DC) signal. The resultant AC signal is recorded as a function of the signal frequency (Barbir, 2005). Gas diffusion, charge-transfer as well as conduction of electrons and protons have different time constants (Yuan et al., 2007). A time constant is a quantity of time expressing the PEFC's speed of response to the perturbation by the AC signal. The complex resistance that must be overcome for each process to occur is termed impedance.

Impedance spectra are conventionally expressed in Nyquist and Bode plots (Wu et al., 2008). This study will only focus on Nyquist plots and therefore Bode plots will not be described. Nyquist plots are complex-plane displays of the imaginary versus real impedance at various frequencies.

The total impedance of a PEFC can be modelled as a combination of different electrical circuit elements, typically but not exclusively resistors and capacitors. If the modelled circuit produces an identical response to that of the PEFC when an AC signal is imposed on it, then it can be labelled as an equivalent circuit (Yuan et al, 2010). Each element in the equivalent circuit represents a specific process that dominates at a certain frequency and or time constant.

Figure 7 shows a Nyquist plot and Randles equivalent circuit with some hindrance to mass-transfer of the gas, known as Warburg impedance, W. From the Nyquist plot, the ohmic resistance, R_s, charge-transfer resistance, R_{CT}, double layer capacitance (C_{dl}) and the Warburg impedance can be determined. The ohmic resistance and charge-transfer resistance are read-off the real axis of the Nyquist plot. The diameter of the semi-circle is equal to the charge transfer resistance.

Gebregergis, Pillay and Rengaswemy (2010) used EIS to distinguish between a normal, flooded and dehydrated PEFC. It was found that the response of the normal and flooded states displayed one semi-circle on the Nyquist plot while that for the dehydrated cell states showed two semi-circles or arcs. Figure 8 illustrates the result they obtained.

Ohmic resistance and charge transfer resistance have been investigated by fuel cell developers using EIS.

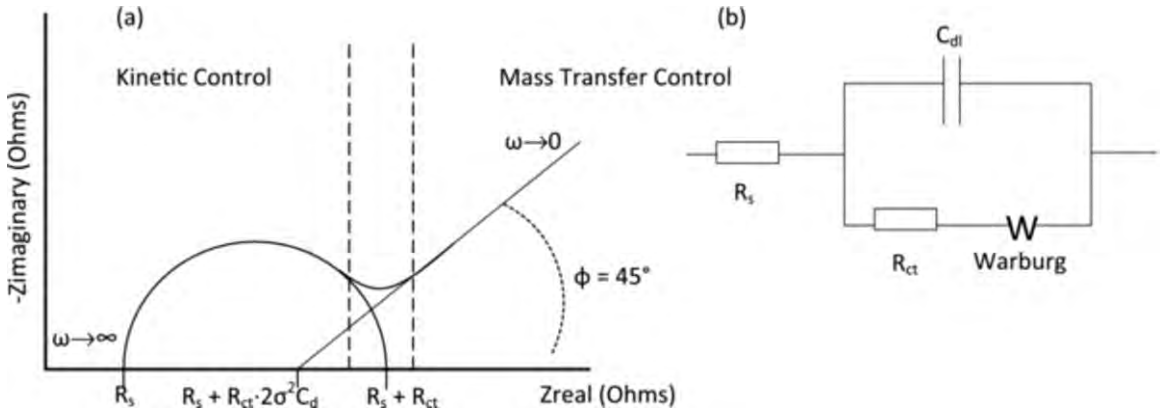

Figure 7: (a) Nyquist plot example & (b) Randles Circuit with Warburg element (Yuan et al., 2010)

Le Canut et al. (2009) showed that the ohmic resistance decreases as the cell compression pressure increases. Cha et al. (2006) found that charge-transfer resistance increases as more water accumulates within the PEFC because access to the reaction sites is hindered. In addition Cha et al. (2006) found that GDL thickness affects flooding and therefore the charge-transfer resistance is also be affected by changes in GDL thickness.

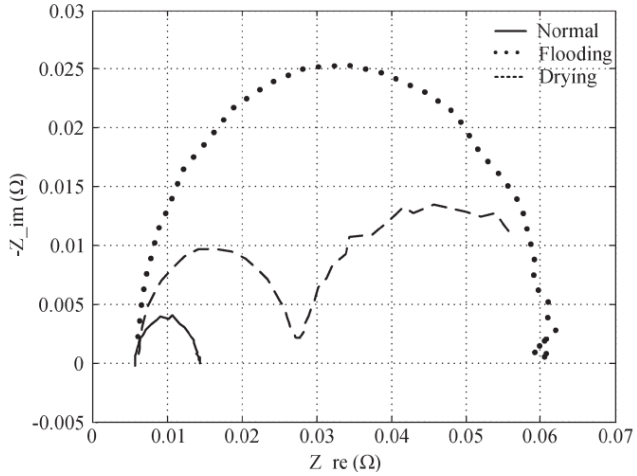

Figure 8: Nyquist plot for a normal, flooded and dehydrated cell (Gebregergis, Pillay & Rengaswemy, 2010)

2.5.3 Pressure Drop

Reactant gases flowing through the flow channels experience pressure drop due to friction between the reactants and flow channels and also due to changes in flow direction, for example in sharp turns (Barbir, 2005). Pressure drop has been used as a parameter to study flooding in the flow channels. Ma et al. (2006) used pressure drop as a diagnostic tool to study water transport in a transparent PEFC. A straight minichannel with an equivalent diameter of 1.2 mm was used. It was found that pressure drop increased as the amount of liquid water present in the flow channel increased. It was also found that the pressure drop sharply declined after the liquid water was discharged from the channel.

Hussaini and Wang (2009) used a pressure drop co-efficient to study water accumulation in a straight or parallel flow field design with minichannels. The minichannels had an equivalent diameter of 667 µm. The pressure drop co-efficient, ϕ_{2p}, is a ratio of the pressure drop measured when current is drawn to that when no current is drawn from the PEFC. Equation 9 shows how the ratio is determined.

$$\phi_{2p} = \frac{\Delta P_{actual}}{\Delta P_{single\ phase}} \qquad \textbf{Equation 9}$$

$\Delta P_{single\ phase}$ was obtained by measuring the ΔP at the open circuit voltage, OCV. At OCV, there is no water generation and the pressure drop observed is due to friction between the reactants and channel walls along the channel length. ΔP_{actual} was measured while drawing a fixed current from the PEFC.

The associated air stoichiometric ratios were varied from 2 to 4 at the cathode side. It was found that ϕ_{2p} approached unity at high stoichiometric ratios and that ϕ_{2p} decreased with increasing air stoichiometry at all the currents tested. A pressure drop co-efficient of unity implies that there is no liquid water or that any liquid water formed from the electrochemical reaction was quickly removed from the PEFC. In addition, this technique could be used to determine the minimum flow rate required to achieve a ϕ_{2p} of unity, and therefore prevent flooding or the onset of flooding from occurring.

3. Objectives of study

Water management is a critical aspect of PEFCs which strongly affects performance and durability. One of the most commonly employed strategies to assist with water removal from the fuel cell is the design and optimisation of the flow field channels. Most commercial fuel cell systems employ flow field channels which can be categorised as minichannels. Minichannels are classified as those having hydraulic diameters ranging from greater than 200 μm to less than 3000 μm. Microchannels refer to channels with diameter of less than or equal to 200 μm. The use of microchannels allows for a simultaneous reduction in the rib or land width of the flow field. The decreased local land area could potentially offer advantages of reduced flooding in the GDL and fuel cell as well as better gas distribution across the active area of the fuel cell. There is limited work on the use of microchannel based flow field designs for PEFCs. Specifically whilst the effect of operating conditions (for improved water management) is well studied for minichannels the same has not been investigated for microchannel based designs.

The primary objective of this study is to investigate the use of a microchannel flow field design (channel width = 200 μm) for a low temperature PEFC with specific focus on:

- Overall fuel cell performance and limiting current density
- Effect of different operating conditions → reactant gas flow rate and cell compression
- Pressure drop behaviour
- Cell voltage behaviour as a function of time

The secondary closely related objective is to compare performance trends of the microchannel flow field design with a commercially available flow field design. This is done to assess whether a microchannel based design behaves in a similar manner to the more conventional minichannel based system when the fuel cell operating conditions are changed. The overarching goal is to develop a more comprehensive understanding of the use of a microchannel based flow field system, with specific focus on water management.

4. Experimental

This section reports a detailed description of the experimental procedure adopted in this study. The details of the MEA and cell components are first provided. The testing setup and procedure used are then outlined and lastly the details of the different diagnostics tests performed are presented.

4.1 Cell Component Description

Table 2 describes the fuel cell components used in this study except the flow field plates. MEAs were prepared using commercial components. Two main types of flow field plates were used and these are described separately in Table 3.

Table 2: Fuel Cell Components

Component	Supplier	Product Code	Description
Catalyst Coated Membrane	Ion Power, Inc., USA	MEA-XL	Catalyst loading- 0.3/0.3 mg cm^{-2} Active area - 25 cm^2
Gas Diffusion Layer	Freudenberg Fuel Cell Component Technologies (FCCT), Germany	H2315 I3 C1	Carbon paper with MPL Average thickness - 260 μm Bulk GDL PTFE loading - 10 wt%
Gaskets	Sanshin Enterprises Co. Ltd, Tokyo, Japan	-	Gasket type – Flat Material – Silicon Thickness - 200 μm
Current Collector Plates	Toyo Precision Parts MFG Co. Ltd, Nara, Japan	-	Material - 316L stainless steel Surface treatment - 100 nm layer of gold
End Plates	Pragma Industries, France	-	Aluminium

Table 3: Flow Field Plates

Flow Field Plate	Microchannel	Commercial
Supplier	Toyo Precision Parts MFG Co. Ltd, Nara, Japan	Pragma Industries, France
Material	Material - 316L stainless steel Surface treatment - 100 nm layer of gold	Graphite
Flow Field Design	Parallel	5-fold multichannel serpentine
Channel Depth	0.1 mm	1 mm
Channel Width	0.2 mm	1 mm
Land Width	0.1 mm	1 mm

Figure 9 illustrates the two flow field designs, namely the microchannel and 5-fold multichannel serpentine design on the commercial flow field plate.

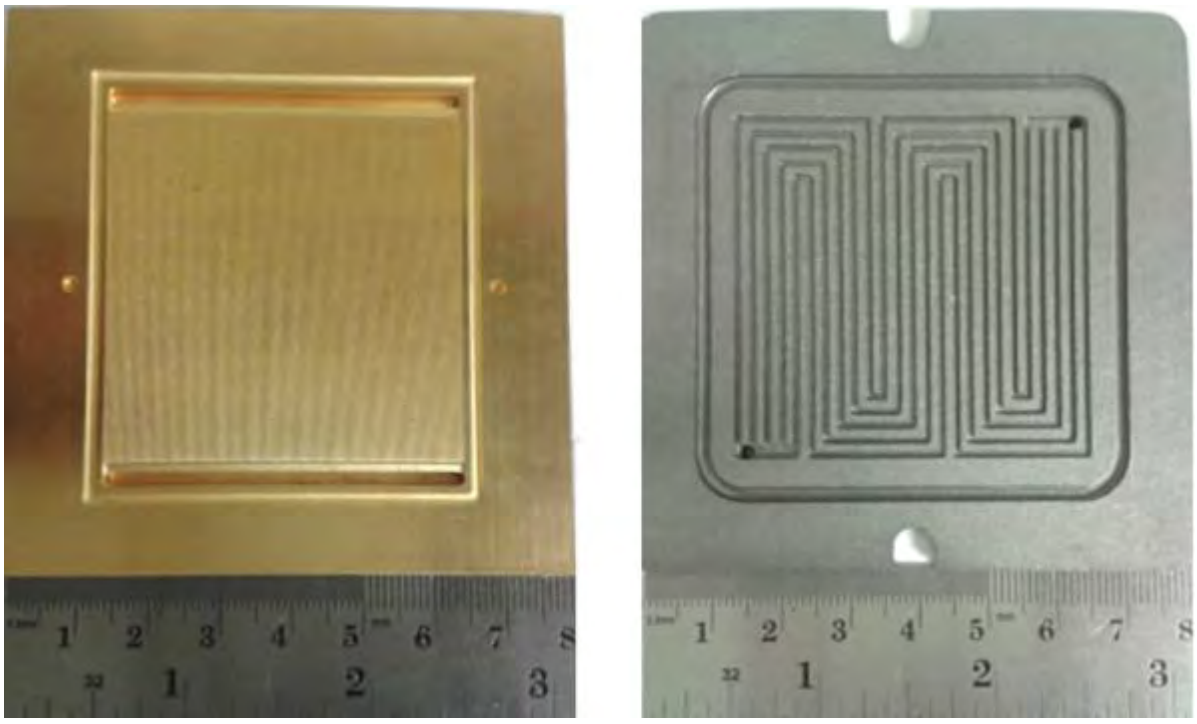

(a) **(b)**

Figure 9: (a) Microchannel and (b) commercial flow field plates

4.2 Testing setup

All fuel cell testing was performed in a single cell setup using the aforementioned cell components. For each test a new set of MEA components and gaskets were used whilst the same flow field plates (either microchannel or commercial), current collector plates and end plates were used for all tests.

Prior to fuel cell assembly the flow field plates were cleaned with iso-propanol and lint free cloth. The end plates have eight holes on the edge of the plates to allow for insertion of tie rods. The tie rods are used to compress the internal fuel cell components by application of a torque on the tie rods.

Fuel cell tests were conducted by connecting the single cell to an Evaluator C50-LT test station from FuelCon. The test station consisted of electronic mass flow controllers, heated and insulated gas feed lines, electrical heating system, temperature control systems, an external humidification system, an electronic load (TrueData-LOAD®), a pressure control system consisting of back pressure regulators and a computerized data acquisition system. All the settings of the test station and fuel cell were monitored and controlled through a data acquisition system connected to a computer running Windows XP Professional SP2 and FuelWork® software. The software allows measurement of voltage-current data in either potentiostatic or galvanostatic mode.

All gases for the testing were provided by pressurised gas cylinders. The supplier and specifications of the gases are provided in Table 4.

Table 4: Description of gas cylinders connected to the test station

Supplier	Gas	Composition
Air Liquide	Nitrogen	99.999% N_2
Air Liquide	Hydrogen	99.999% H_2
Air Products	Synthetic Air	79% N_2 & 21 % O_2

4.3 Summary of fuel cell tests and operating conditions

Table 6 presents the complete list of fuel cell tests conducted. Fuel cell tests were performed for the two different flow fields at three different torques, corresponding to three different cell compressions. The torques of 1, 1.6 and 2.6 Nm were applied on 8 bolts, each with a 5 mm diameter over an area of 64 cm^2. Table 5 reveals the cell compression pressures studied.

Table 5: Cell compression pressures studied

Torque (Nm)	Clamping Force (N)	Cell Compression Pressure (MPa)
1	8 000	1.25
1.6	12 800	2.00
2.6	20 800	3.25

For all fuel cell tests except test 9, 4 different cathode stoichiometries were investigated. For Tests 1-6, the stoichiometric ratios were based on a current of 1.5 Acm^{-2} whilst for Tests 7 and 8 the stoichiometric ratios were load following i.e. based on the current being drawn from the fuel cell.

Test 9 was conducted to determine the main contributor (increase in oxygen partial pressure vs. increased drag force to push out water) to the performance increase as the cathode stoichiometry increases. The basis for test 9 was to keep one of the contributors constant and to vary the other one. Test 9 therefore involved maintaining a constant drag force whilst varying the oxygen partial pressure. This was achieved by varying the cathode operating (back) pressure at a fixed cathode stoichiometric ratio of 2, to achieve the same partial pressure as would be experienced for a stoichiometric ratio of 4. Table 7 summarises the cathode pressures used in test 9.

Table 6: Overview of fuel cell tests and operating conditions

Test #	Flow field	Torque / Nm	Operating conditions					Diagnostic tests
			T / ^{o}C	P / bar	RH / %	s_{anode}	$s_{cathode}$	
1	Microchannel	1	80	1	100%	1.5 @ 1.5 Acm^{-2}	2, 2.5, 3 & 4 @ 1.5 Acm^{-2}	• Polarization curves • High frequency resistance • Electrochemical impedance spectroscopy at 0.25 and 1.2 Acm^{-2}
2	Microchannel	1.6						
3	Microchannel	2.6						
4	Commercial	1						
5	Commercial	1.6						
6	Commercial	2.6						
7	Microchannel	1.6				1.5	2, 2.5, 3 & 4	• Pressure drop co-efficient measurements • Cell voltage monitoring
8	Commercial	1.6						
9	Microchannel	1.6		Anode - 1 Cathode- Varying*		1.5	2	• Polarization curves • High frequency resistance

NB. T = temperature, P = Pressure, RH = Relative Humidity of anode and cathode,
s_{anode} = stoichiometry of anode, $s_{cathode}$ = stoichiometry of cathode.
*described in Table 6

Table 7: Cathode pressures for Test 9

Stoichiometric Ratio	Oxygen Partial Pressure (bar)	Required operating pressure at stoichiometric ratio of 2 (bar)
2.0	0.108	1.00
4.0	0.148	1.18

4.4 Fuel cell testing procedure and diagnostic measurements

This section outlines the testing procedure and diagnostic measurements conducted for all the fuel cell tests listed in section 4.3. All tests were subjected to the pre-test diagnostics and start-up and conditioning (section 4.4.2). Following this, tests 1-6 were subjected to polarization curve and electrochemical impedance spectroscopy measurements (sections 4.4.3 and 4.4.4) whilst test 7 and 8 were subjected to pressure drop co-efficient and cell voltage monitoring measurements (sections 4.4.5 and 4.4.6). For test 9 only polarization curves were conducted.

4.4.1 Pre-test diagnostics

Prior to any fuel cell testing and operation of the test station a leak test was performed with nitrogen on both anode and cathode to ensure the gaskets were sealing the fuel cell. The leak test was done by feeding nitrogen to both anode and cathode compartments of the fuel cell with the exhaust of the two compartments closed. Once a gauge pressure of 0.5 bar had built up the inlet valves of the both the anode and cathode were closed to trap the nitrogen pressure slightly above atmospheric. The drop in the pressure of the trapped nitrogen was then used as measure for a leak in the system. A maximum pressure drop of 0.05 bar over a 5 minute interval was deemed acceptable.

Following the leak test a voltammeter was connected to the end-plates to check if there was any current that could leak from the current collector plate to the end-plates due to insufficient insulation between them.

4.4.2 Start-up and conditioning

The fuel cell was started up by incrementally increasing the cell temperature from room temperature to the desired cell temperature of 80^{o}C. During the heat up period nitrogen was purged at a volumetric flow rate of 25 Nl/min through both anode and cathode. Flow through the humidifiers was activated immediately and the temperature of the humidifiers was such that it was always at least 5^{o}C less than the cell temperature. Once the cell temperature reached the desired set point the humidifier temperatures were then set to the same as the cell temperature to achieve

100% RH. The feed lines that connect the humidification system to the fuel cell were set at 120^{o}C in order to avoid any water condensation from occurring prior to the fuel cell.

When the cell temperature was 10^{o}C less than the final desired temperature, hydrogen and air were fed to the anode and cathode respectively. The different gases (nitrogen vs hydrogen and air) have different heat capacities and the 10^{o}C allowance was necessary to prevent temperatures from overshooting during the switch over. The flow rates of hydrogen and air corresponded to stoichiometry of 1.5 and 2 at 1.2 Acm^{-2} respectively.

Once the desired operating conditions were achieved, the fuel cell was conditioned using a procedure outlined by the CCM manufacturer, Ion Power Inc. The conditioning procedure was conducted in potentiostatic mode such that the voltage was cycled between 0.8 V and 0.3 V. The voltage was held for 30 seconds at 0.8 V and for 10 minutes at 0.3 V. At the end of each cycle the current and high frequency resistance (conducted at 10 kHz) were measured and recorded at 0.3 V. Twelve cycles were conducted resulting in a 2 hour rapid conditioning or break in procedure. Twelve cycles were found to be suitable to achieve steady state fuel cell performance in terms of the current measured at the end of each cycle.

4.4.3 Polarization Curve

Polarization curves were conducted in galvanostatic mode. Prior to starting the polarization curves the appropriate stoichiometry was set at the first value for both anode and cathode as presented in section 4.3 The current was then stepped up incrementally from OCV to the maximum specified current and the voltage at each current was recorded after a three minute wait period. Three voltage measurements were recorded every ten seconds after the three minute stabilization period between current set-points. An average voltage was then calculated for each current density set-point tested. The maximum specified current for testing with air was 50 A corresponding to 2 Acm^{-2}. After the voltage measurements were completed, high frequency resistance (HFR) measurements were conducted at 10 kHz.

The incremental current step varied depending on which region of the polarization curve was being measured. In the activation region (from OCV to 0.1 Acm^{-2}) the current increment was 0.02 Acm^{-2}, whilst for the ohmic and mass transfer regions (> 0.1 Acm^{-2}), the incremental step was 0.08 Acm^{-2}. In the case that the fuel cell did not reach the aforementioned maximum specified current (2 Acm^{-2}) a lower voltage limit of 0.3 V was chosen to prevent the fuel cell from operating at very low voltages which could have led to other reactions such as carbon support corrosion and platinum dissolution. The polarization curve was repeated according the procedure just described.

Following two polarization curves at a specific stoichiometry, the cathode stoichiometry was increased as described in section 4.3 and the above measurement repeated. In all, a total of 8 polarization curves were conducted corresponding to two polarization curves at each cathode stoichiometry (2, 2.5, 3 and 4).

4.4.4 Electrochemical Impedance Spectroscopy

Electrochemical impedance spectroscopy (EIS) measurements were performed at two different current densities (0.25 Acm^{-2} and 1.2 Acm^{-2}) immediately after the polarization curve measurements. The fuel cell was made to operate at each current density for 30 minutes prior to the EIS measurement.

EIS measurements were performed by perturbing the fuel cell system with a sinusoidal (AC) current of known amplitude in the frequency range of 0.1 – 10 000Hz with 8 steps per decade. The resulting AC amplitude and response of the cell was monitored and recorded.

4.4.5 Pressure Drop Measurements

Pressure drop measurements from the inlet to the exit of the fuel cell cathode side were conducted for tests 7 and 8 (as outlined in section 4.3) immediately following the start-up and conditioning steps. Pressure drop measurements were conducted at four different current densities of 250, 500, 750 and 1 000 $mAcm^{-2}$. At each current density the pressure drop was measured at four different cathode flow rates corresponding to stoichiometries of 2, 2.5, 3 and 4. This produced a total of 16 measurements. The pressure drop was also measured when no current was flowing and each of the 16 flow rates. From the pressure drop measurements a pressure drop co-efficient was calculated by dividing the pressure drop at a specific current and flow rate over the pressure drop when no current was being drawn and at the same flow rate. The idea was to obtain a measure of the pressure drop due to the removal of liquid water.

For the pressure drop measurements when a current was being drawn, the fuel cell was first made to operate at that current for 25 minutes. The pressure drop measurement was then recorded every ten seconds over a five minute interval and an average pressure drop was calculated. For the measurement when no current was being drawn the waiting period was only five minutes with a subsequent three minute interval for measurement of the average pressure drop. This was done to avoid overexposure of the fuel cell to an open circuit voltage condition.

4.4.6 Cell Voltage Monitoring Measurements

Following the pressure drop measurements, voltage monitoring measurements were conducted. Prior to the measurement any residual water in the channels was removed by purging with high flow rates of hydrogen and air (~ s = 1.5/2 at 2 Acm^{-2}), while operating the fuel cell at a low current density of 0.25 Acm^{-2}. The measurements involved operating the fuel cell at a constant current and monitoring the cell voltage over 150 minute periods. The cell voltage was recorded every 100 milliseconds to observe the behaviour of the cell voltage over time. The measurements were conducted at three different current densities corresponding to 0.25 Acm^{-2}, 0.5 Acm^{-2} and 1 Acm^{-2}. At each current density, measurements at four different cathode stoichiometries (2, 2.5,3 and 4) were conducted.

5. Results and Discussions

This section presents the results and discussion of this study. The effect of the cathode flow rate and cell compression on fuel cell performance is first presented. This is followed by the results of the pressure drop experiments and lastly the cell voltage monitoring experiments. All results are discussed with specific reference to water build-up and removal in the fuel cell.

5.1 Effect of Cathode Flow Rate

5.1.1 Microchannel flow field

Figure 10 shows the effect of varying the cathode stoichiometric ratio on the polarization curve performance and high frequency resistance in the microchannel flow field design (Test 2 in section 4.3 – All test conditions available as fold out page in appendix). The bolt torque was 1.6 Nm. For the polarization curve measurements the cathode stoichiometric ratio is the ratio at a specific current density, i.e. at 1.5 Acm^{-2} as shown in Table 5. Therefore the cathode flow rate is not load following and is constant for the whole polarization curve.

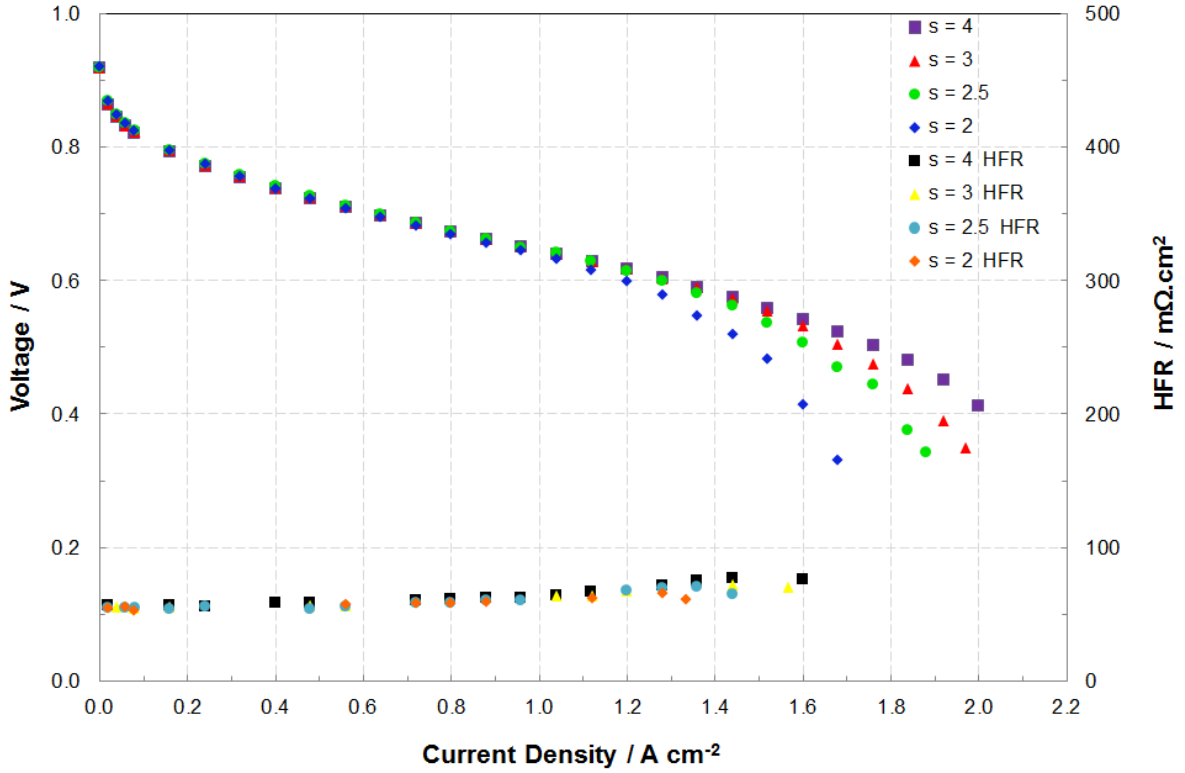

Figure 10: Effect of varying cathode stoichiometry on polarization curve performance and high frequency resistance (HFR) for test 2

Figure 10 reveals that as the cathode stoichiometric ratio was increased from 2 to 4 there was a negligible influence on the polarization curve performance and high frequency resistance to a

current density of 1.2 Acm^{-2}, corresponding to the activation and ohmic controlled regions. Above 1.2 Acm^{-2} the difference in polarization curve performance becomes substantial with improved performance as cathode stoichiometric ratio increased. This result is expected and the trend is in agreement with results in the literature for conventional minichannel based flow field designs (Kim, Shimpalee & Van Zee, 2004; Kumbur, Sharp & Mench, 2006; Gerteisen et al., 2012). The limiting current is typically defined as the point at which the cell voltage drops vertically and is a good indication of severe mass transfer limitations within the fuel cell, predominantly as a result of severe flooding. Figure 10 shows that the limiting current increases as the cathode stoichiometric ratio increases. This result is also in agreement with the findings of Williams, Kunz and Fenton (2004) for conventional minichannel based flow field designs.

The trend in polarization curve performance and limiting current density with increasing cathode stoichiometric ratio is due to two main factors – (i) an increase of the oxygen partial pressure in the cathode catalyst layer and (ii) an increase in the drag force to remove liquid water in the cathode flow channels. The trend is therefore as expected but the degree of improvement with cathode stoichiometric ratio may be different from conventional minichannels and this will be compared and discussed later in Figure 16.

The high frequency resistance was for most part independent of the cathode flow rate, although at current densities above 1.4 Acm^{-2}, the higher stoichiometric ratios appear to show a marginally higher resistance. The slightly higher resistance can be attributed to the fact that at the higher stoichiometric ratios the removal of excess water due to increased drag force may have caused a slightly reduced saturation level of the membrane.

Figures 11 and 12 show EIS results at 0.25 and 1.2 Acm^{-2}, respectively. By fitting a Randles equivalent circuit to the EIS data, the ohmic resistance and Faradaic or charge transfer resistance can be determined. These are shown for both current densities in Table 7.

Table 8 shows that the ohmic resistances at both current densities do not change much with a change in cathode stoichiometric ratio from 2-3.5. A marginal increase is observed for a stoichiometric ratio of 4. This result is in agreement with the high frequency resistance measurements during the polarization curve measurements and can be explained by a slight decrease in membrane saturation at the highest flow rate.

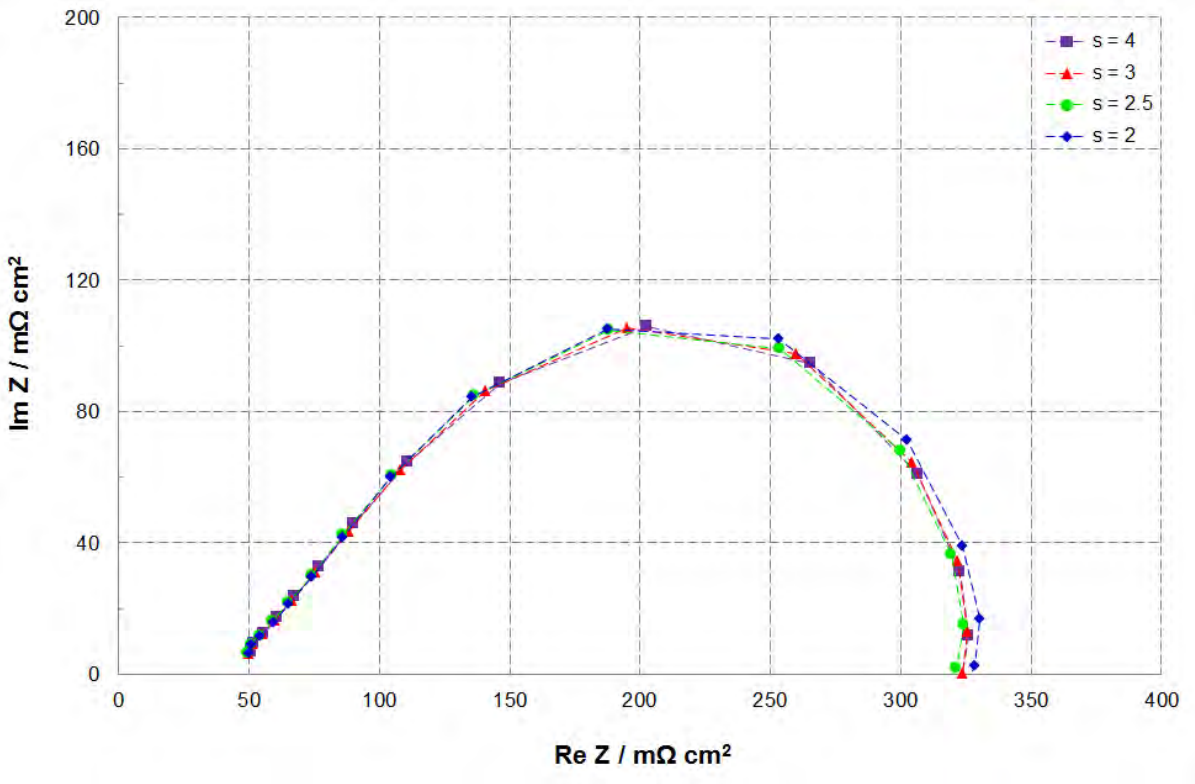

Figure 11: Nyquist plot at 0.25 Acm^{-2} for test 2 - varying cathode flow rates in microchannel flow field

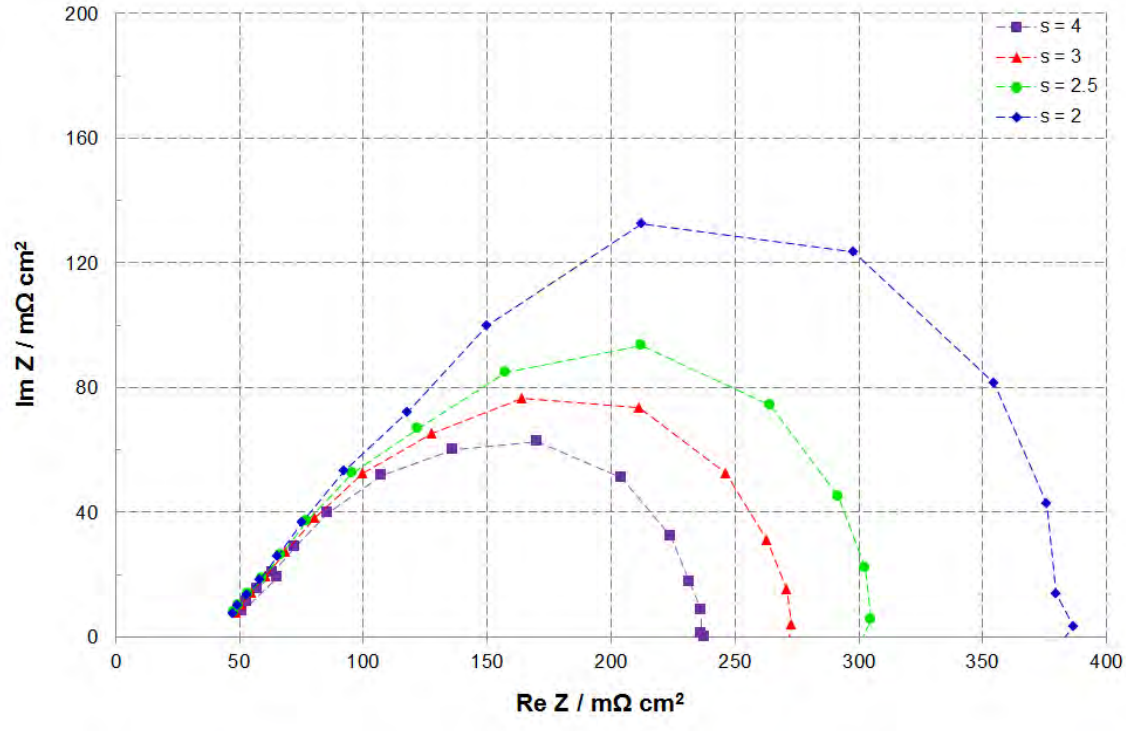

Figure 12: Nyquist plot at 1.2 Acm^{-2} for test 2 - varying cathode flow rates in microchannel flow field

Table 8: Faradaic and ohmic resistances in mohm cm^2 at two different current densities for microchannel flow field at 1.6 Nm

Stoichiometric ratio	0.25 Acm^{-2}		1.2 Acm^{-2}	
	Ohmic	Faradaic	Ohmic	Faradaic
2	50.0	328	47.5	386
2.5	49.7	321	48.0	304
3	50.2	323	50.7	272
4	50.7	323	51.8	237

The values of Faradaic resistances at 0.25 Acm^{-2} are very close and this is in line with similar polarization curve performance at this current density. At 1.2 Acm^{-2} there is a clear trend of decreasing Faradaic resistance as stoichiometry increases. The higher oxygen partial pressure and the improved water removal (and therefore less water build-up) as stoichiometric ratio increases may both contribute to the improved Faradaic resistance. It can be argued that the higher oxygen partial pressure may be having a minimal effect since no difference is being observed at 0.25 cm^{-2} (rate of water production is low at this current density so water build-up is not likely). This is possible but the partial pressure effect becomes more important at 1.2 Acm^{-2}, where the reaction rate is much higher and mass transfer rate of oxygen becomes limiting. The increase of Faradaic resistance as a measure to indicate water build-up in microchannels has been reported (Cha et al., 2004). Furthermore, the result is also similar to the findings of Yuan et al. (2010), who reported that an increase in oxygen partial pressure would reduce the resistance to charge-transfer. The difference in the Faradaic resistances at 1.2 Acm^{-2} is to an extent in line with difference in the polarization curve results at the same current density, although the difference in the former is far more pronounced.

5.1.2 Commercial flow field

Figure 13 shows the effect of varying the cathode stoichiometry on the polarization curve performance and high frequency resistance in the commercial flow field design (Test 5 in section 4.3). The bolt torque was 1.6 Nm.

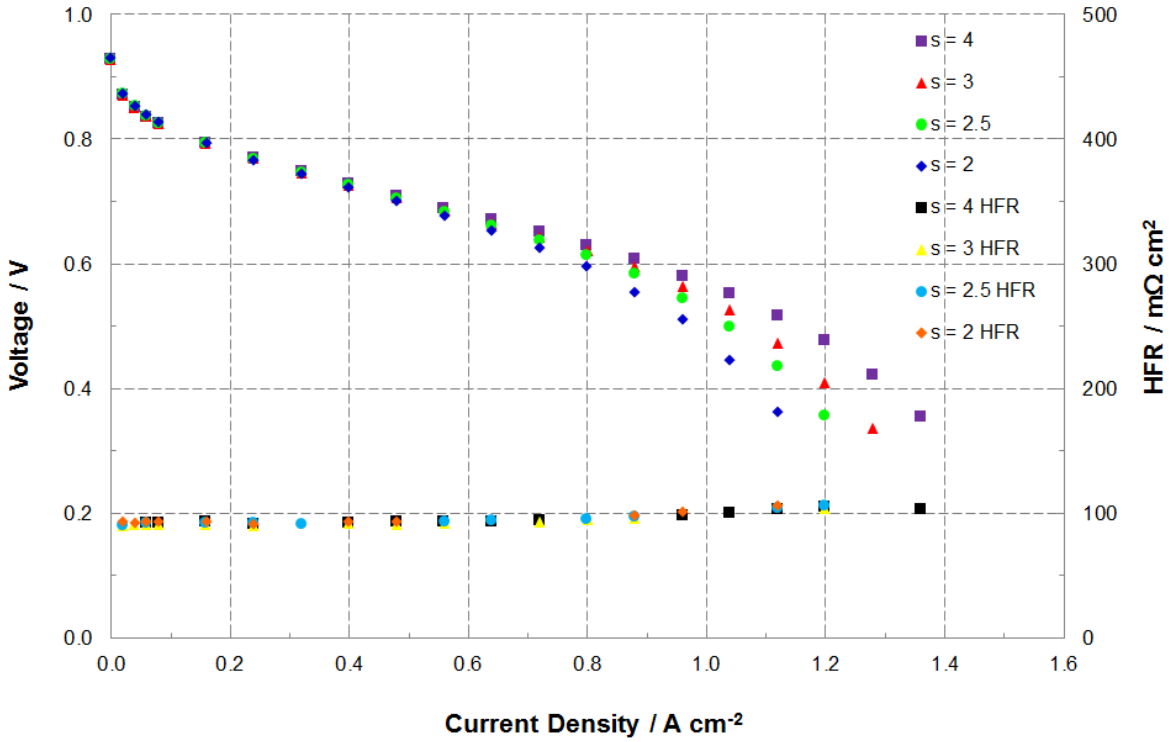

Figure 13: Effect of varying cathode stoichiometry on polarization curve performance and high frequency resistance (HFR) for test 5

Figure 13 shows a very similar trend to the microchannel flow field design with similar polarization curve performance for all stoichiometric ratios at low to medium current densities whilst at higher current densities the performance increases as the stoichiometric ratio increases. Figure 13 also shows that the high frequency resistances were almost identical for all the stoichiometric ratios tested, indicating that for commercial flow field design, the increased water removal at higher flow rates is having negligible effect on the water saturation of the membrane. This could also imply that in the commercial minichannel based flow field design, not as much water gets removed at the higher flow rate vs. the lower flow rate, compared to the microchannel flow field design. A full comparison of trends between the microchannel and commercial flow fields is discussed later in section 5.1.3.

Figures 14 and 15 show EIS results at 0.25 and 1.2 Acm^{-2}, respectively. Once again, by fitting a Randles equivalent circuit to the EIS data, the ohmic resistance and Faradaic resistances can be determined and these are shown in Table 9.

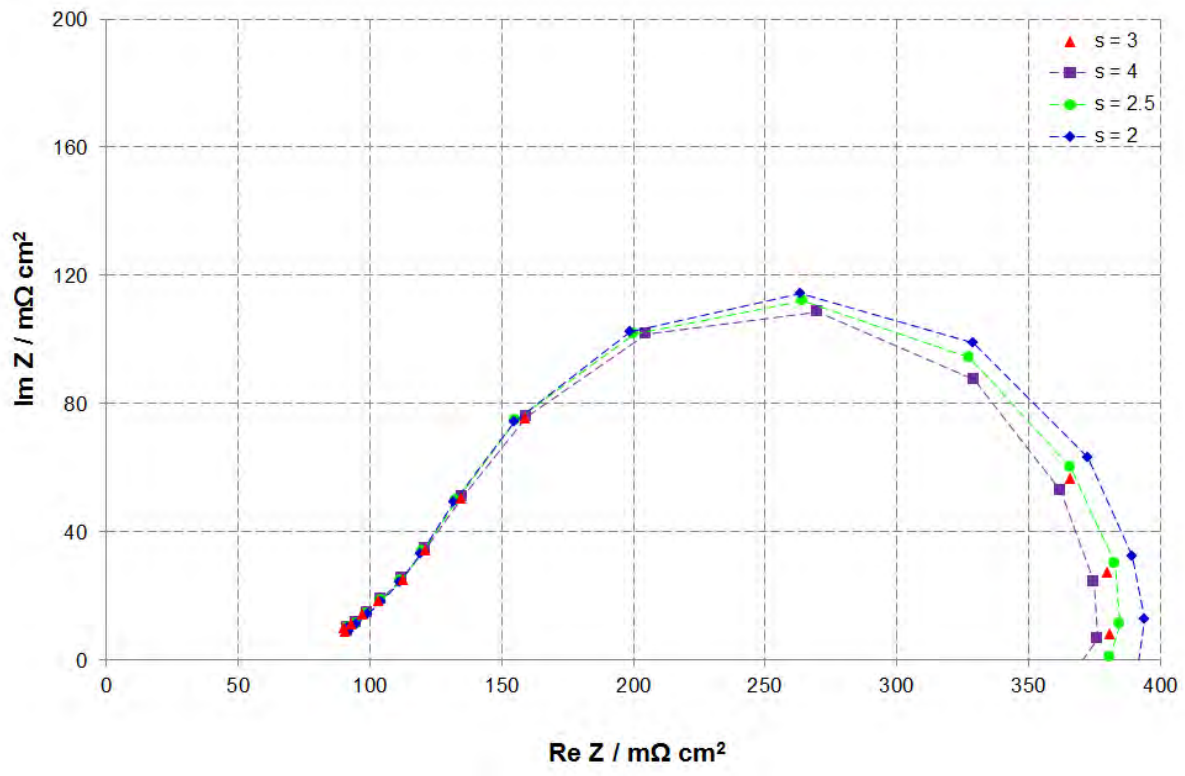

Figure 14: Nyquist plot at 0.25 Acm^{-2} for test 5 - varying cathode flow rates in commercial flow field

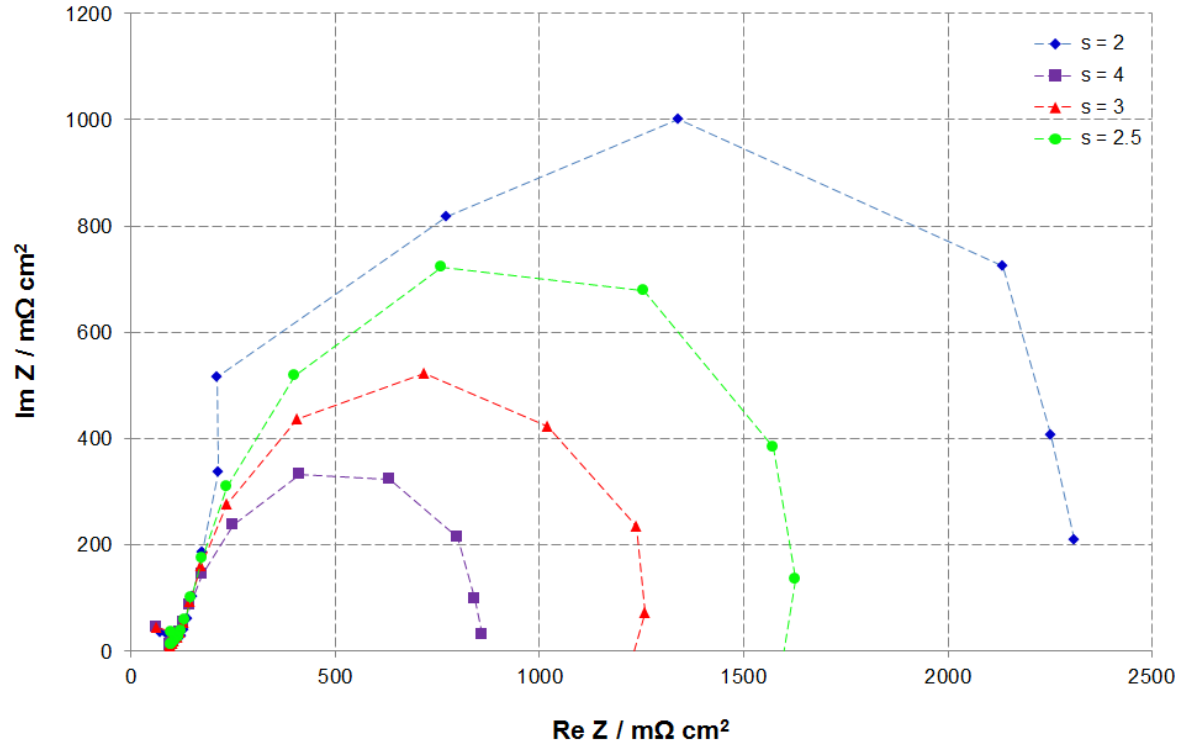

Figure 15: Nyquist plot at 1.2 Acm^{-2} for test 5 - varying cathode flow rates in commercial flow field

Table 9: Faradaic and ohmic resistances in mohm cm^2 at two different current densities in commercial flow field at 1.6 Nm

Stoichiometric ratio	0.25 Acm^{-2}		1.2 Acm^{-2}	
	Ohmic	Faradaic	Ohmic	Faradaic
2	91.8	394	105	2310
2.5	91.5	381	100	1630
3	90.3	378	101	1260
4	91.5	376	99.8	862

Table 8 shows that the Faradaic resistance decreases with increasing stoichiometric ratio at both current densities. The difference is less at 0.25 Acm^{-2} and does not relate directly to the polarization curve where the performance appears very similar at the same current density. The results suggest that even at the lower current density, the commercial minichannel design is affected by differences in the cathode flow rate and therefore the different partial pressures and drag forces.

5.1.3 Comparison of trends of microchannel and commercial flow field designs

Figures 16 and 17 compare the trends of limiting current and Faradaic resistance with varying cathode stoichiometric ratio or flow rate for the two flow field designs. For both flow field designs the limiting current increases as the cathode stoichiometric ratio increases. This result implies that the microchannel shows the same expected trend as the commercial flow field.

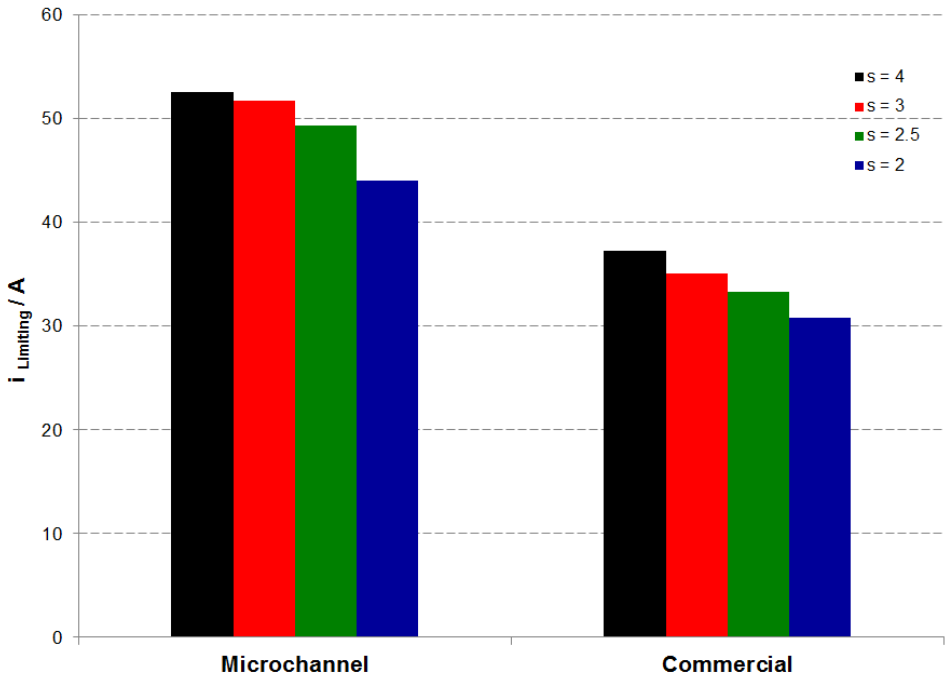

Figure 16: Limiting current at for varying cathode stoichiometric ratios for the microchannel and commercial flow field designs

The increase for the commercial flow field design is more regular or gradual whilst for the microchannel design the initial difference from a stoichiometry of 2 to 2.5 is significantly more than the other step increases. This result shows that the microchannel design is more sensitive to changes in the stoichiometric ratio at higher current densities. This may imply that it is easier to remove water from the microchannels by increasing the flow compared to the commercial flow field channels. Given that the channel width of the microchannel is 5 times less than the commercial one, the size of the water droplets in the microchannels will be considerably smaller. Therefore for the same drag force it should be easier to remove water from the microchannels than the commercial minichannels. An additional explanation for the lower sensitivity of the commercial flow field to changes in stoichiometry may be that flooding in this system may not be in the channels but rather in the GDL. This is very possible given the fact that the commercial flow field has a larger land or rib width (1 mm) which is an order of magnitude higher than the microchannel flow field rib width (0.1 mm). Flooding in fuel cell systems employing conventional minichannels such as those present in the commercial flow field are known to most commonly occur in the GDL under the land areas of the flow field (Cha et al., 2004).

Figure 17 shows that the Faradaic resistance increases as the cathode stoichiometric ratio decreases for both flow field designs. The increasing resistance is far less pronounced for the microchannel design, although the larger difference from a stoichiometric ratio of 2 to 2.5 is in agreement with the results of the trend in the limiting current.

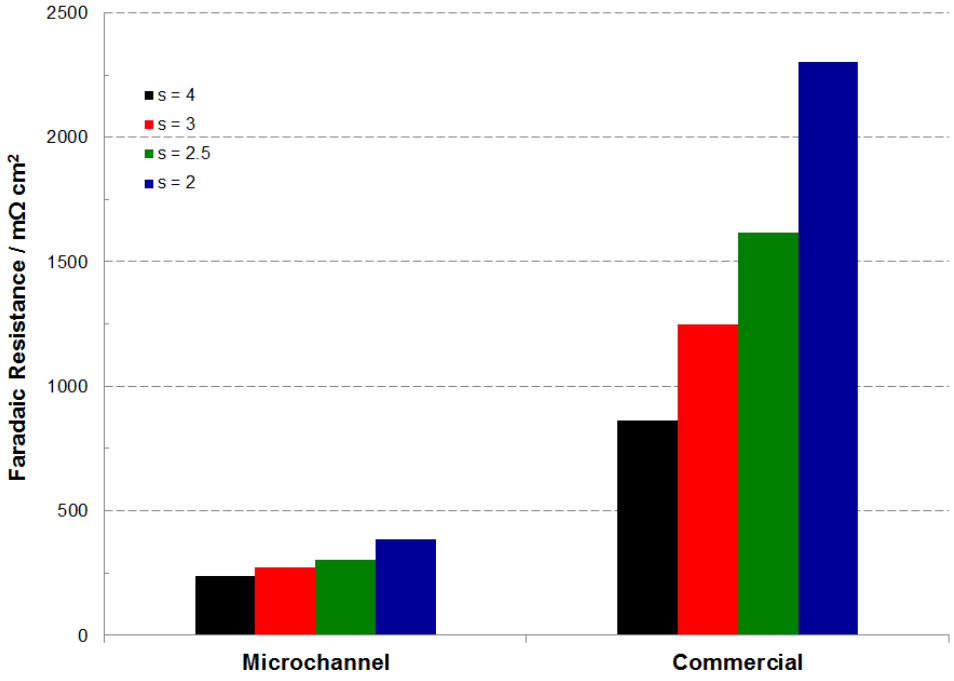

Figure 17: Faradaic resistance for varying cathode stoichiometric ratios for the microchannel and commercial flow field cells designs at 1.2 Acm^{-2}

5.1.4 Oxygen partial pressure vs. drag force

Figure 18 shows polarization curve and high frequency resistance results of Test 9. In addition the result of the highest stoichiometric ratio from test 2 (s=4) is also superimposed on the graph. This test was conducted to determine the main contributor (increased oxygen partial pressure vs. increased drag force to push out water) to the performance increase as the cathode stoichiometric ratio increases in the microchannel design. Test 9 ensured that the drag force was constant but the oxygen partial pressure varied. Figure 18 indicates that there is a slight improvement in performance due to the increase in oxygen partial pressure (s=2 and P = 1bar vs. s=2 and P = 1.18 bar). However the improvement in performance does not match the performance of the highest stoichiometric ratio (s=4).

The result confirms that the performance increased when the stoichiometric ratio increased, as expected, a combination of both the increase in oxygen partial pressure and an increase in drag. However given that there is only a slight improvement with an increase in oxygen pressure, it can be argued that the major contributor to the performance increase is the increased drag force. It can also be argued that above a current density of 1.5 Acm^{-2}, the performance increase is for the most part due to the increased drag force. This result is of interest for the operation protocol of a system employing a microchannel flow field design. More specifically if the operating current density is below 1.5 Acm^{-2} then using a stoichiometric ratio of 4 (and therefore higher load on an upstream compressor to achieve this extra flow) will not improve performance significantly compared to a lower stoichiometric ratio. In other words only if the operating current density is above 1.5 Acm^{-2} will the flow rate need to be adjusted. This result also supports the argument made to explain the trend in the limiting current for the microchannel design, viz. the microchannel flow field experiences water build-up in the channels (as opposed to the in the GDL) and this is removed by increasing the cathode flow rate.

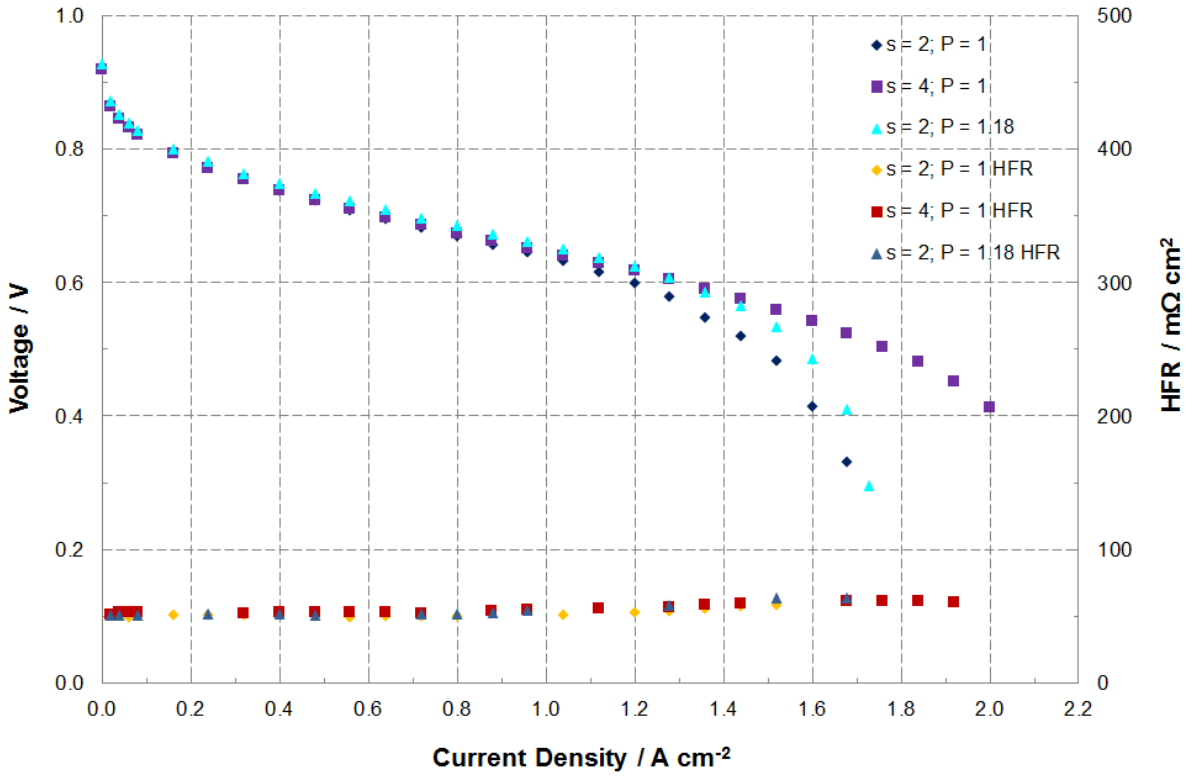

Figure 18: Polarization curve and high frequency resistance (HFR) for a fixed cathode stoichiometry and varying cathode operating pressure in the microchannel flow field design. The result of s = 4 is superimposed for comparative purposes

5.2 Effect of Cell Compression

5.2.1 Microchannel flow field

Figures 19 and 20 show the effect of varying the cathode stoichiometric ratio on the polarization curve performance and high frequency resistance in the microchannel flow field design (Tests 1 and 3) for a bolt torque of 1 and 2.6 Nm respectively. For both torques, the performance in the medium to high current density increases as stoichiometric ratio increases. Subsequently the limiting current also increases as the stoichiometric ratio increases. For the torque of 1.0 Nm, the limiting currents are significantly lower than at 2.6 Nm. A discussion of the trends in limiting current and other parameters is presented in section 5.2.3 in addition to a comparison of the results of the commercial flow field.

Figure 21 presents the EIS results at 0.25 Acm^{-2} and 1.2 Acm^{-2} at torques of 1 Nm and 2.6 Nm. Similar to the results obtained at 1.6 Nm (section 5.1) the Faradaic resistances increase with decreasing stoichiometric ratio at the higher current density of 1.2 Acm^{-2}, whilst minimal difference is seen at the lower current density of 0.25 Acm^{-2}.

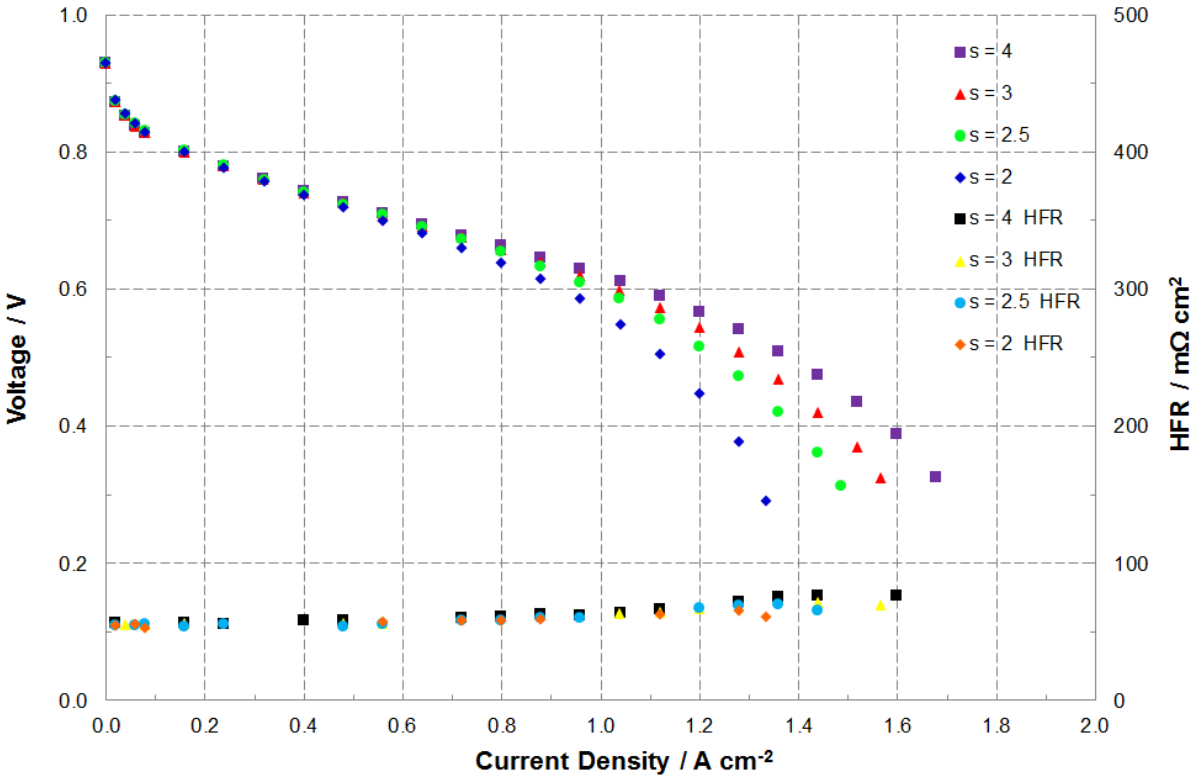

Figure 19: Effect of varying cathode stoichiometry on polarization curve performance and high frequency resistance (HFR) in the microchannel flow field at a bolt torque of 1 Nm (Test 1)

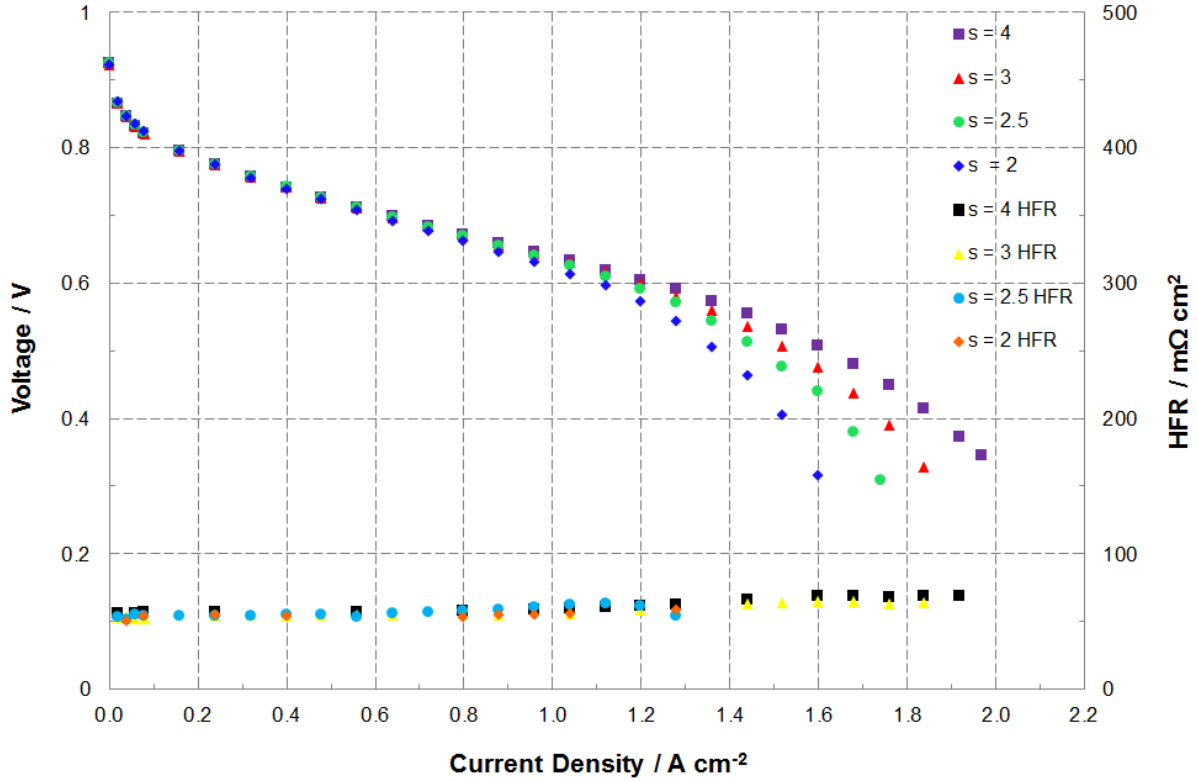

Figure 20: Effect of varying cathode stoichiometry on polarization curve performance and high frequency resistance (HFR) in the microchannel flow field at a bolt torque of 2.6 Nm (Test 3)

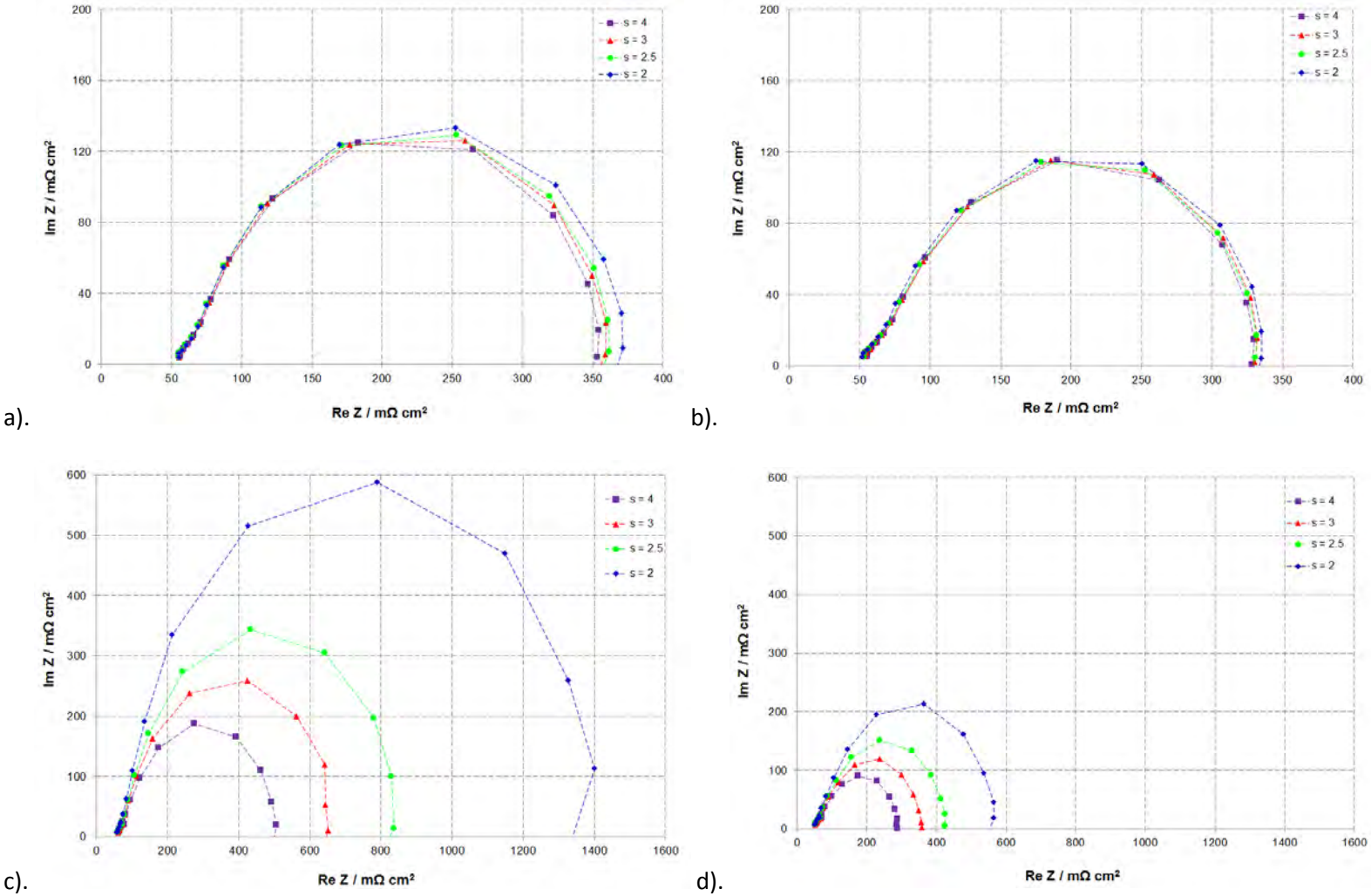

Figure 21: Nyquist plots in the microchannel flow field at; a). 1 Nm & 0.25 Acm^{-2}, b). 2.6 Nm & 0.25 Acm^{-2}, c). 1 Nm & 1,2 Acm^{-2} and d). 2.6 Nm & 1.2 Acm^{-2}

5.2.2 Commercial flow field

Figures 22 and 23 show the effect of varying the cathode stoichiometric ratio on the polarization curve performance and high frequency resistance in the commercial flow field design (Tests 4 and 6) for a bolt torque of 1 Nm and 2.6 Nm respectively. Whilst the general trend of improved performance with increasing stoichiometric ratio at the high current densities is still observed the improvement in performance is considerably less than that in the microchannel flow field design.

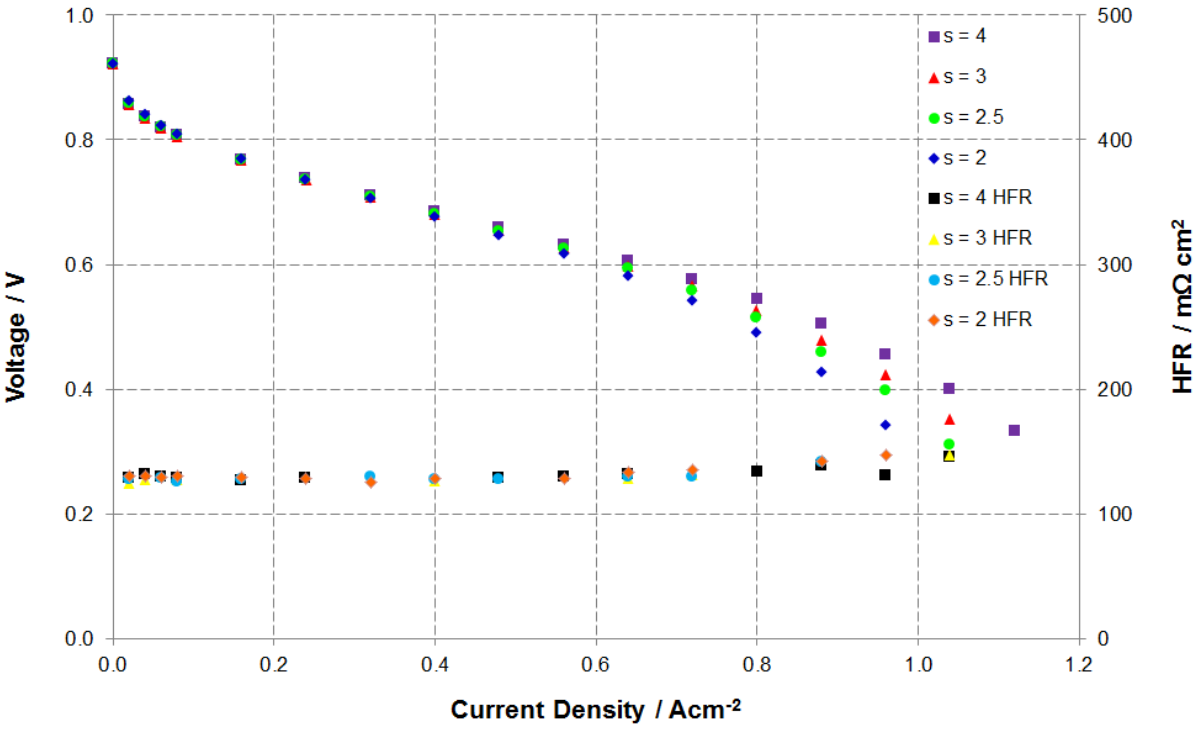

Figure 22: Effect of varying cathode stoichiometry on polarization curve performance and high frequency resistance (HFR) in the commercial flow field at a bolt torque of 1 Nm (Test 4)

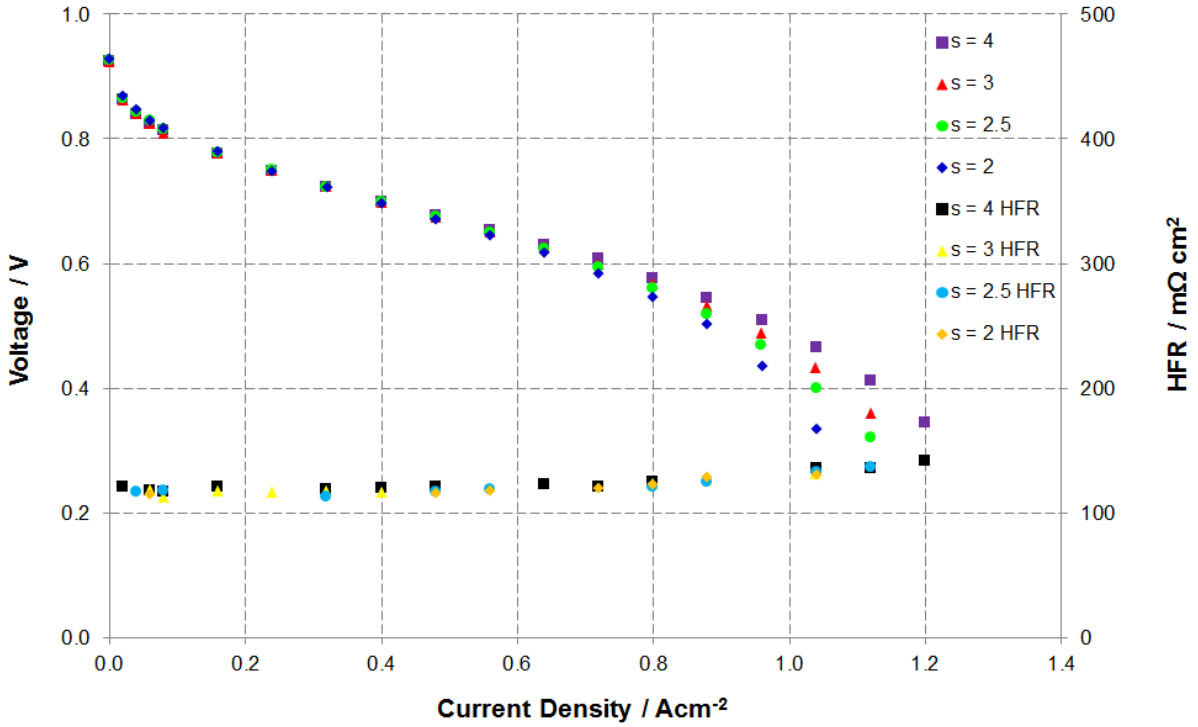

Figure 23: Effect of varying cathode stoichiometry on polarization curve performance and high frequency resistance (HFR) in the commercial flow field at a bolt torque of 2.6 Nm (Test 6)

Figure 24 presents the EIS results at 0.25 Acm^{-2} at torques of 1 Nm and 2.6 Nm. EIS measurements at 1.2 Acm^{-2} were conducted but no stable results were obtained and this is not surprising given that at both torques and for all stoichiometric ratios the limiting current from the polarization curves was found to be less than or in one case equal to 1.2 Acm^{-2}.

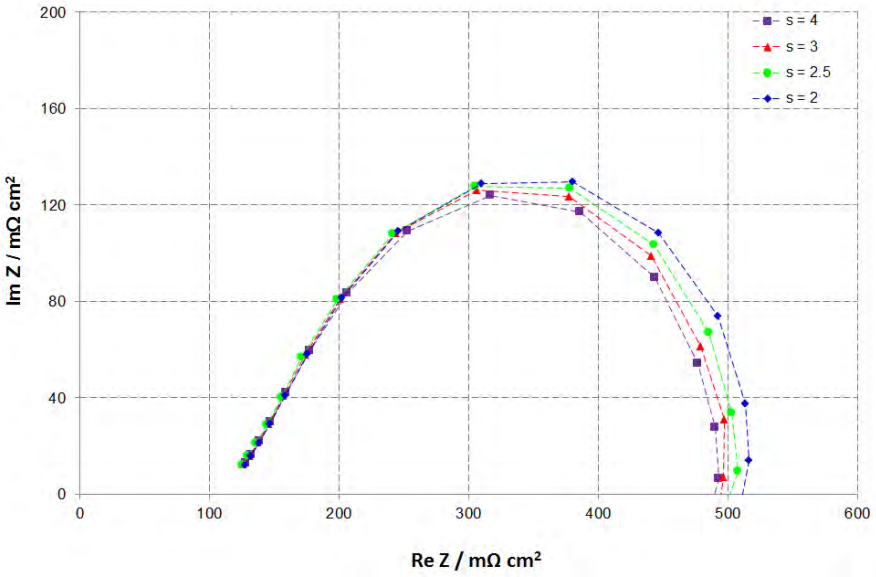

a).

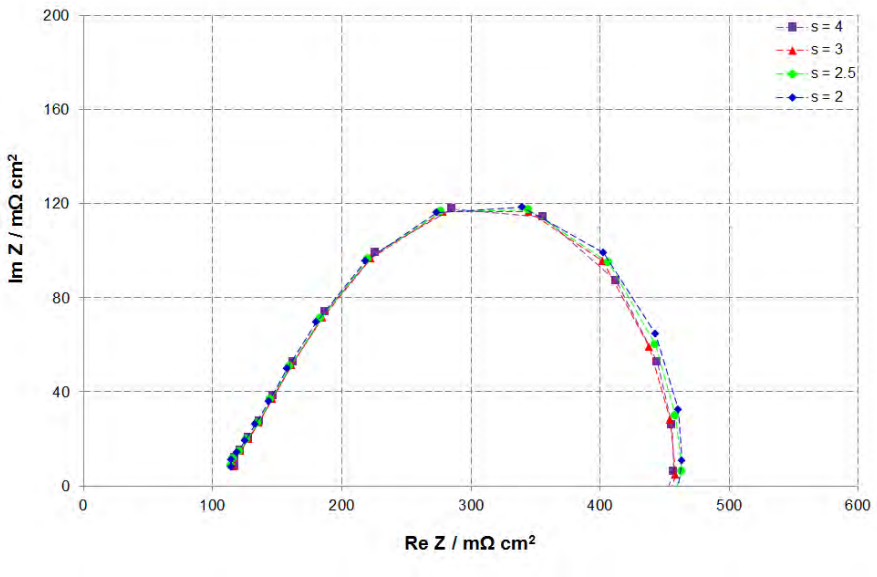

b).

Figure 24: Nyquist plots in the commercial flow field at; a). 1 Nm & 0.25 Acm^{-2}, b). 2.6 Nm & 0.25 Acm^{-2}

5.2.3 Comparison of trends of microchannel and commercial flow field designs

At all torques, the microchannel design is more sensitive to changes in the flow rate and therefore changes in the drag force. This once again suggest that water build-up for the microchannels is in the channels and not the GDL. In the case of the commercial flow field design, the fact that the performance in the high current density region is not very sensitive to cathode flow rate, specifically at the highest torque, further confirms the notion that most of the build-up or flooding effects for the commercial design takes places in the GDL.

Figure 25 compares ohmic resistance as a function of the cell compression for the microchannel and commercial flow field at a current density of 0.25 Acm^{-2} and a cathode stoichiometric ratio of 2. For both designs the lowest resistance was observed at the middle torque of 1.6 Nm. This can be rationalised since at a bolt torque of 1 Nm the contact between the different cell components is not sufficient resulting in a high contact resistance, whilst at too high a bolt torque of 2.6 Nm the cell compression may be uneven resulting in poor contact in the middle areas of the active area. The difference in the resistances show that the commercial flow field is far more sensitive to bolt torque than the microchannel flow flied. This suggests that the distribution of the cell torque across the active area is far better for the microchannel design compared to the commercial design resulting in less sensitivity to different cell torques. The commercial flow field has a conventional land or rib width of 1 mm. The microchannel design on the other hand has a land width an order of magnitude lower, specifically 0.1 mm. Thinner land widths and therefore more frequent land sections per unit length appear to provide better distribution of the cell torque across the fuel cell active area.

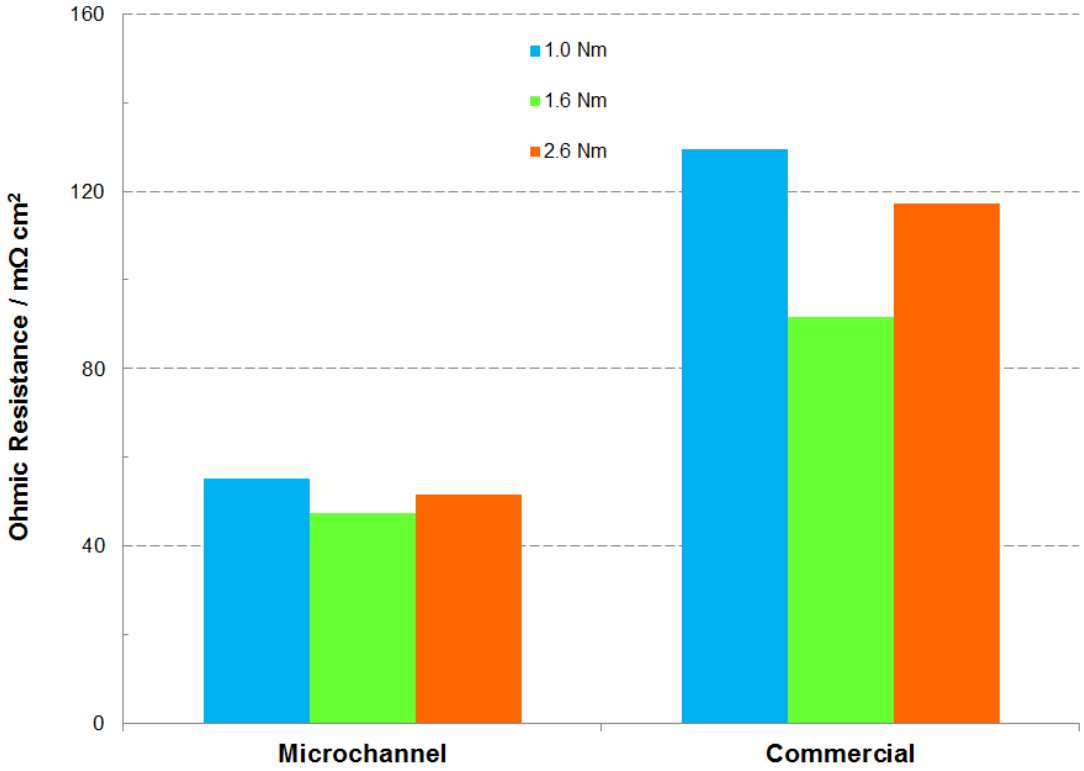

Figure 25: Ohmic resistance as a function of cell compression for the microchannel and commercial flow field at a current density of 0.25 Acm^{-2} and a cathode stoichiometric ratio of 2

Figure 26 compares the limiting current as a function of the cell compression for the microchannel and commercial flow field at a current density of 0.25 Acm^{-2} and a cathode stoichiometric ratio of 2. The results show that the same trend for both flow field designs with the highest limiting current in both cases being observed for the intermediate torque of 1.6 Nm. The worst result at 1 Nm can be closely related to the high ohmic resistances observed at this lowest torque. The limiting current is predominantly affected by the mass transfer limitations within the system such as flooding. The flooding as previously mentioned can be anywhere in the catalyst layer, GDL or flow channels. However it can also be affected by the ohmic resistance since a very high resistance results in increased voltage losses which in turn can result in an impact on voltage drop. At the highest torque, over-compression of some parts of the GDL may lead to increased flooding which may explain a lower limiting current than at a torque of 1.6 Nm.

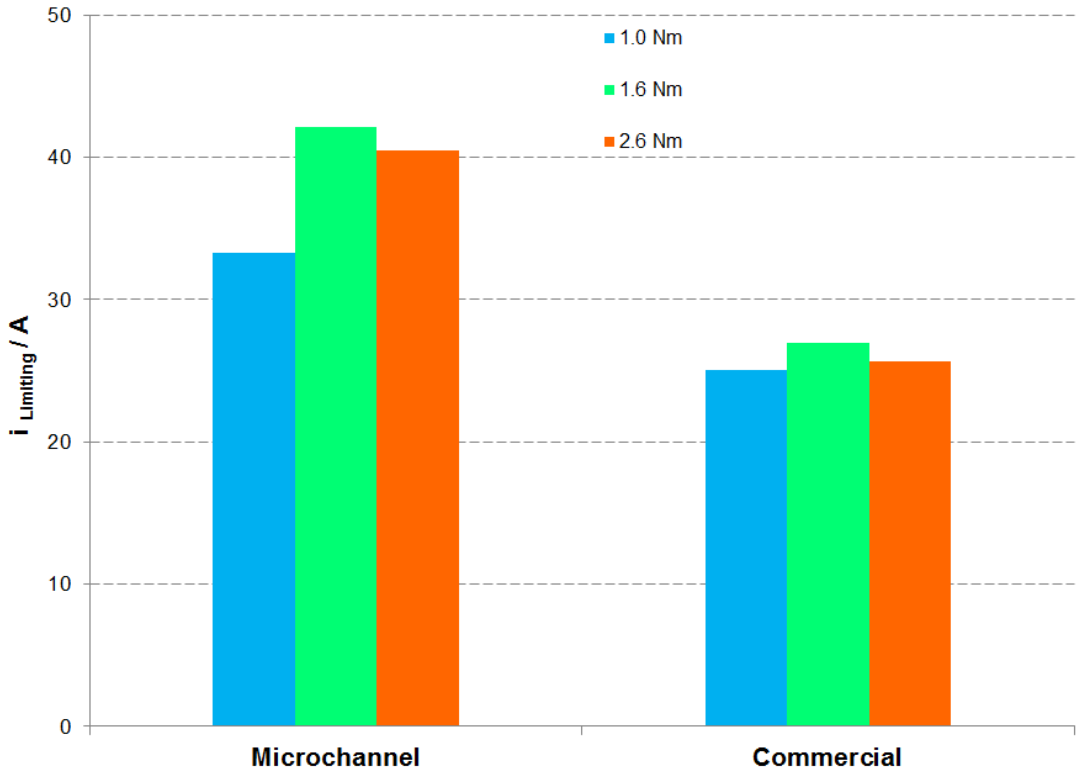

Figure 26: Limiting current as a function of cell compression for the microchannel and commercial flow field at a current density of 0.25 Acm^{-2} and a cathode stoichiometric ratio of 2

5.3 Pressure Drop Behaviour

Figure 27 shows the pressure drop co-efficient as a function of the stoichiometric ratio at four different current densities for the microchannel flow field design (Test 7 in section 4.3). Unlike the polarization curve measurements, the cathode flow rates in the pressure drop measurements were load following (as indicated in Table 5) and therefore increased as the current density increased.

Figure 27 shows that for all current densities a trend of decreasing pressure drop co-efficient as the stoichiometric ratio increases was observed. At a lower stoichiometric ratio and therefore a lower cathode flow rate, the drag force to push out any liquid water in the channels is less. The resulting higher presence of liquid water at the lower stoichiometric ratio results in greater resistance to gas flow causing the greater the pressure drop. The fact that the pressure drop co-efficient decreased significantly from the lowest to the highest stoichiometry (essentially an average slope in the graph) clearly points out to the removal of liquid water in the channels.

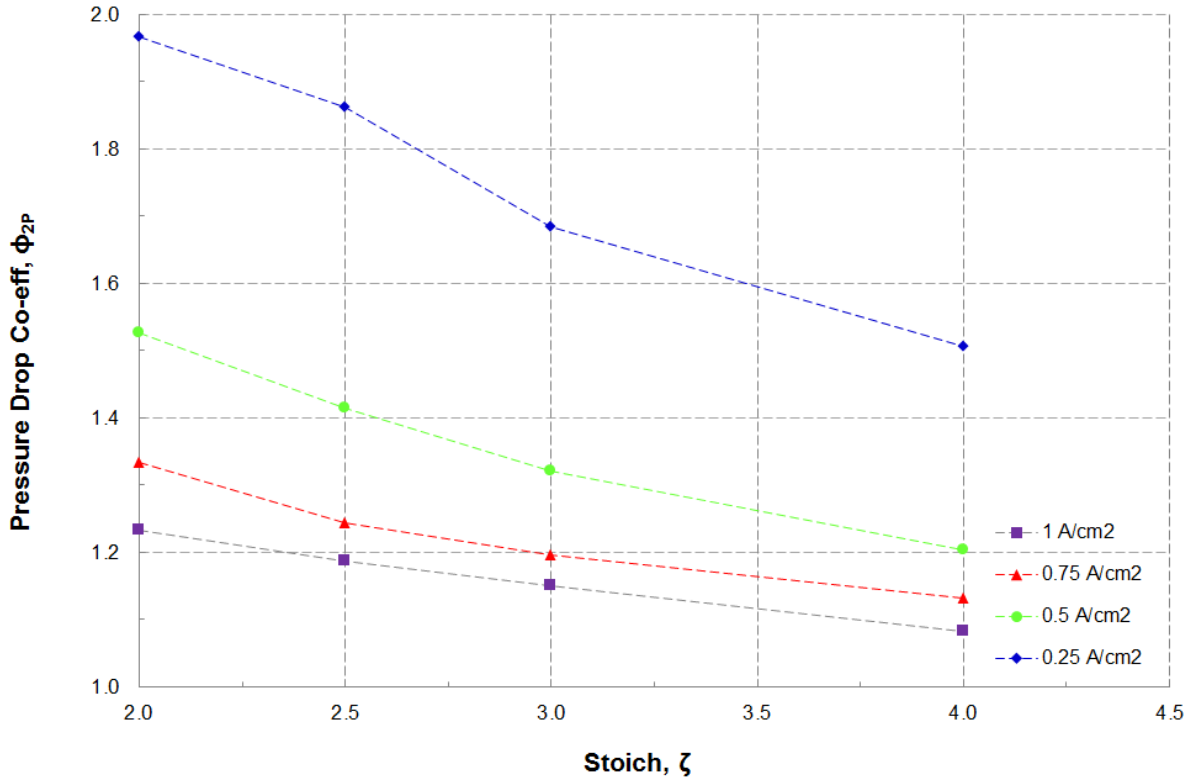

Figure 27: Two-phase pressure drop co-efficient at different current densities in microchannel flow field design

The effect of the change in stoichiometric ratio on the pressure drop co-efficient becomes less as the current density increases. This is interesting since even though at the higher current densities there is more water, the higher total flow rate of gas and therefore higher drag force is clearly the dominating factor. This is confirmed by the fact that for all stoichiometric ratios, the highest pressure drop co-efficient observed was for the lowest current density. More specifically at each stoichiometric ratio the pressure drop co-efficient decreased with an increasing current density. This supports the previously mentioned statement that the magnitude of the drag force (dependant on the absolute total gas flow rate) has a strong influence on the amount of water present in the channels.

Figure 28 shows the pressure drop co-efficient as a function of the stoichiometric ratio at four different current densities for the commercial flow field design (Test 8 in section 4.3). The general trend of a decreasing co-efficient with increasing stoichiometric ratio at all current densities is once again observed. However there were few cases at the lower stoichiometric ratios where the pressure drop increased slightly with increasing stoichiometric ratio. Unlike the microchannel flow field design, the pressure drop co-efficient did not decrease significantly with increasing stoichiometric ratio. Furthermore the pressure drop co-efficient values are a lot closer to unity for the commercial flow field design across all conditions tested. This points towards less water build-up

in the channels of the commercial flow field design compared to the microchannel design. An alternative interpretation could be that the microchannel design is far more sensitive to the build-up of liquid water. In other words the smaller size of the microchannel means water build-up occurs more easily than the larger channels of the commercial flow field design (Cha et al., 2004). Furthermore, the commercial flow field plate in this study is made of graphite whereas the microchannel flow field plate is made of stainless steel. The contact angle of water on graphite is higher than that on stainless steel and therefore build-up of water on graphite based channels is less favourable than metal based channels.

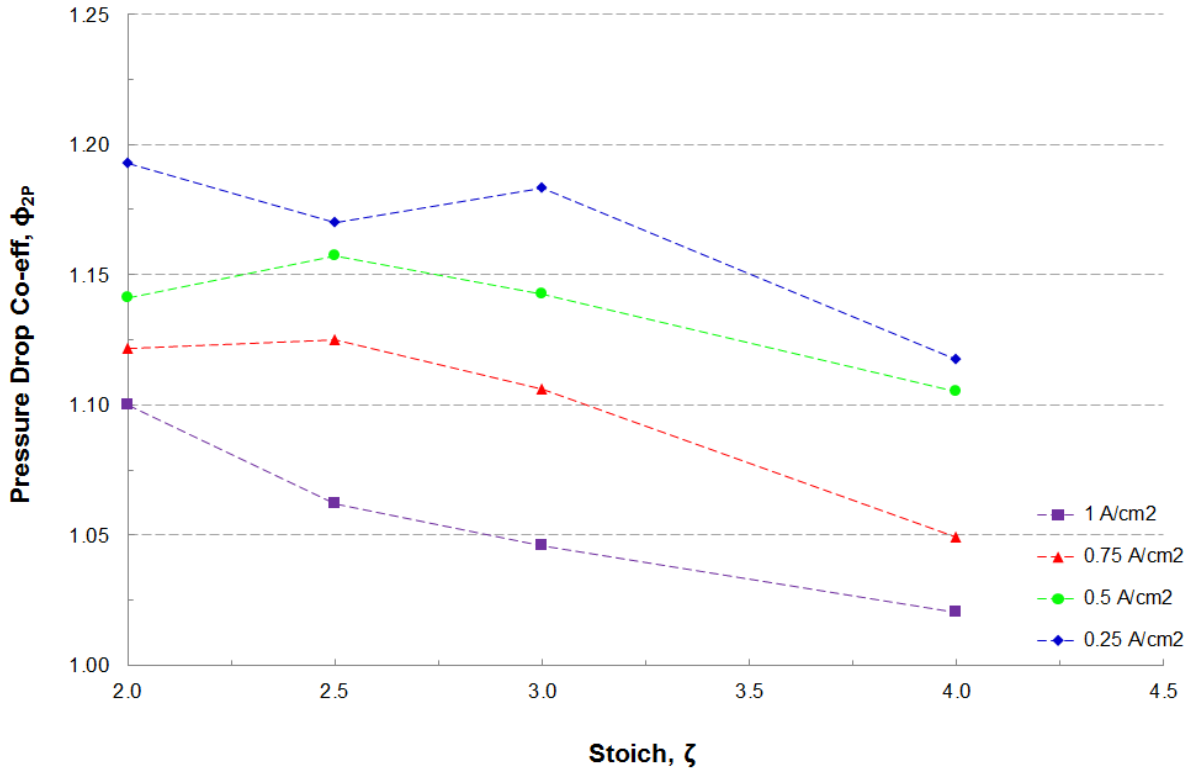

Figure 28: Two-phase pressure drop co-efficient at different current densities in commercial flow field design

The results from both flow field designs show very similar trends to similar experiments on the pressure drop co-efficient in the literature (Hussaini and Wang, 2009). A combined analysis of the results suggests that the there is more water build-up in the channels for the microchannel design. This does not necessarily mean there is no water build-up in the fuel cell for the commercial flow field design. In fact the combination of the pressure drop measurements and polarization curve results (which show inferior performance for the commercial flow field and signs of earlier onset of flooding in the fuel cell) suggest that for the commercial flow field design most of the flooding is occurring in the GDL and not the channels. This is not surprising given that the rib width of the commercial flow field is an order of magnitude higher that the microchannel and flooding in the GDL

under the land area is known to be the most common region of flooding for flow field designs such as the commercial design (Kumar & Reddy, 2003; Cha et al., 2004). The fact that the microchannel design performs so much better in the polarization curve also means that the effect of GDL flooding on performance is far more significant than channel flooding. It also means that whilst the microchannel design shows characteristics of flooding in the channels, the design significantly reduces flooding in the GDL.

5.4 Cell Voltage Fluctuations

Figure 29 shows the cell voltage as a function of time at four different stoichiometric ratios and three different current densities for the microchannel flow field design. Similar to the pressure drop measurements the cathode flow rates were load following and therefore dependant on the operating current density.

The results show very similar performance (cell voltage) for the 4 stoichiometric ratios at a current density of 0.25 and 0.5 Acm^{-2}. In addition the frequency and pattern of the cell voltage fluctuations are very similar. The similar performance is not surprising and agrees with the very similar performance seen in the polarization curve at these current densities. The cell voltage fluctuations are indicative of flooding. Typically the greater the flooding the greater the severity of the fluctuations both in terms of the frequency and size (peaks/troughs) of the fluctuations. The fluctuations could be as result of flooding in any of the catalyst layer, GDL or flow field.

At a current density of 1 Acm^{-2} a performance difference is observable with, as expected, improved performance as stoichiometric ratio increases. There is however no considerable reduction in the size or frequency of the fluctuations as stoichiometric ratio increases. The size of the fluctuations increase slightly in comparison to the lower current densities. This suggests more flooding at the higher current density which is as expected given the higher rate of water production. It is important to point out that these results do not contradict the pressure drop measurement results from section 5.3 since the pressure drop measurement results are purely a function of water in the channels whilst the cell voltage measurements results are influenced by, as previously mentioned, water build-up in any of the catalyst layer, GDL or flow field.

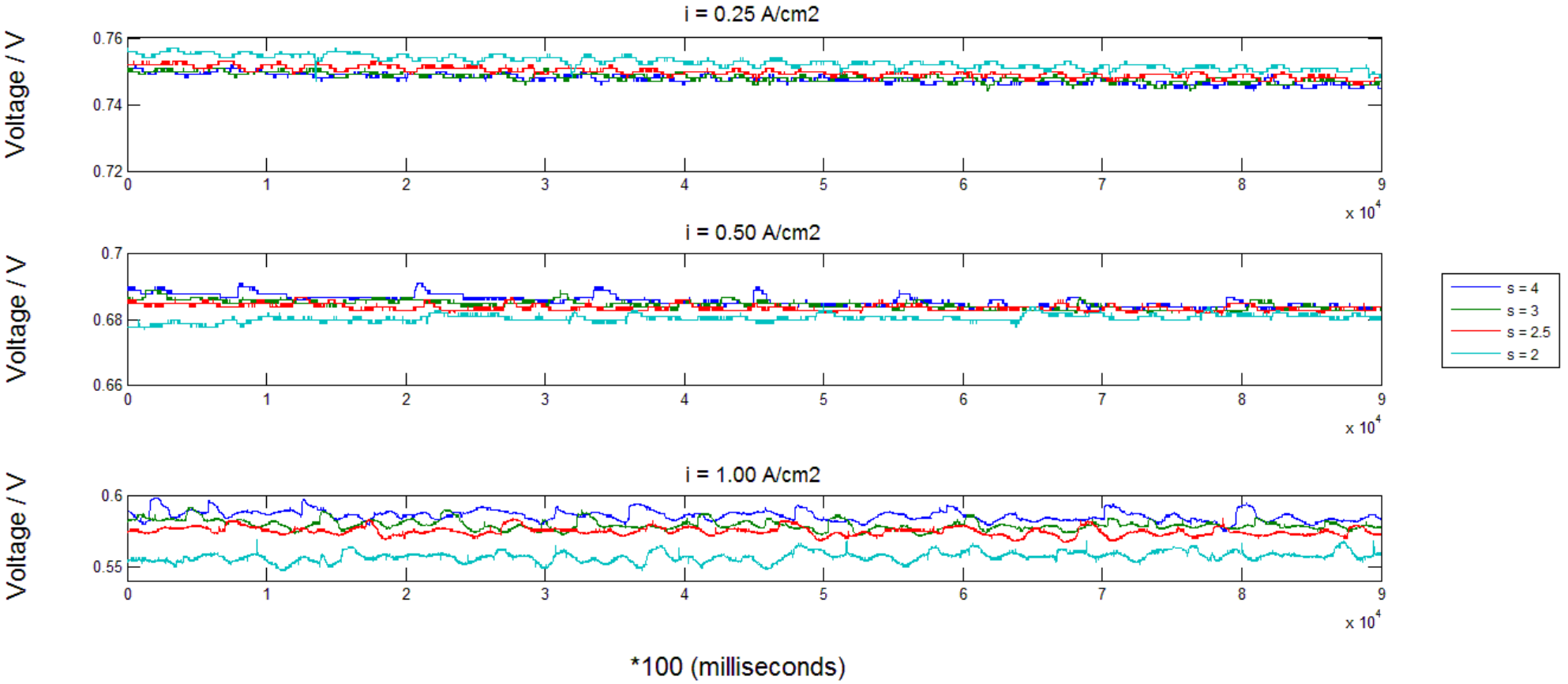

Figure 29: Cell voltage as a function of time for different stoichiometric ratios and current densities in the microchannel flow field

Figure 30 shows the cell voltage as a function of time at four different stoichiometric ratios and three different current densities for the commercial flow field design. Unlike the microchannel design, the performance difference at different stoichiometric ratios starts becoming observable at a lower current density region of 0.5 Acm^{-2}. There is also a significantly bigger difference in performance across the four stoichiometric ratios at a current density of 1 Acm^{-2} compared to the microchannel design. Another notable difference in comparison to the microchannel design is the increased frequency of the fluctuations specifically at the lower stoichiometric ratios. For all three current densities, the size of the fluctuations decreases considerably as the stoichiometric ratio increases. In general the higher frequency and bigger size of the fluctuations for the commercial flow field design clearly point towards a greater degree of water build-up flooding.

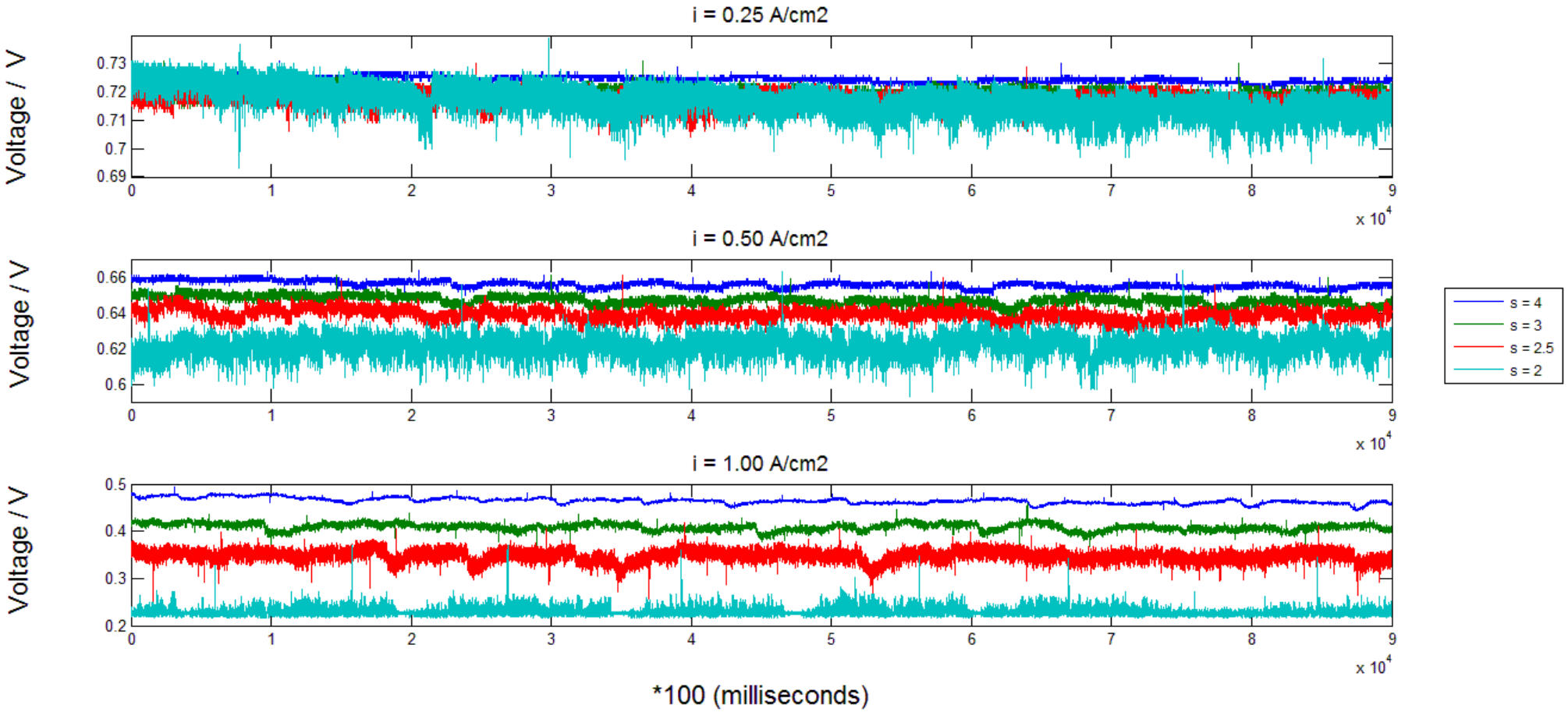

Figure 30: Cell voltage as a function of time for different stoichiometric ratios and current densities in the commercial flow field

6. Conclusions and Recommendations

6.1 Conclusions

This study has investigated the use of a microchannel flow field design for a low temperature PEFC. A summary of the main findings are as follows:

- The microchannel flow field design showed a similar trend (polarization curve and limiting current) to a commercial minichannel based system when the cathode flow rate was changed. Specifically the limiting current increased as cathode flow rate or cathode stoichiometric ratio increased.
- The microchannel flow field design was more sensitive to changes in the cathode flow rate at high current densities at all cell compressions. This implies that it is easier to remove water from the fuel cell using the microchannel system in comparison to the commercial minichannel system.
- The increased performance sensitivity to the flow rate suggests water build-up for the microchannel flow field design is predominantly in the channels and not the GDL, as is typically the case with conventional minichannel based systems.
- The lower sensitivity of the commercial minichannel flow field design suggested that most of the water build-up or flooding effects for the commercial design took place in the GDL.
- The dominating contribution to the performance increase when increasing the cathode flow rate for the microchannel design was found to be the increased drag force to remove water and not the increase in the oxygen partial pressure.
- The ohmic resistance of the microchannel flow field design was less sensitive to changes in cell compression than the commercial minichannel system. This confirmed that the distribution of the cell compression across the active area was superior for the microchannel design and this was attributed to the thinner land width and therefore more frequent land sections per unit area.
- The pressure drop co-efficient measurements showed a significant decrease in the co-efficient with increasing cathode flow rate for the microchannel flow field design whilst for the commercial design the decrease was relatively less and the co-efficient was closer to unity.

- Cell voltage measurements show more fluctuations (frequency and size) at all the conditions tested for the commercial flow field design compared to the microchannel design. This indicated towards a degree of flooding in the fuel cell employing the commercial minichannel system.

The combined analysis of all the results strongly suggested that most of water build-up for the fuel cell using the microchannel flow field design was in the flow channels whilst for the fuel cell with the commercial minichannel design the water build-up was predominantly in the GDL. This coupled with the fact that the fuel cell with commercial minichannel design revealed a greater degree of flooding implied that water build-up in the GDL was a stronger contributor to mass transfer limitations than water build-up in the flow channels. It also meant that whilst the microchannel design showed characteristics of flooding in the channels, the design significantly reduced flooding in the GDL.

6.2 Recommendations

This study has developed a better understanding of the operation of a fuel cell using a microchannel flow field design. Specifically useful information and knowledge of water build-up and flooding in a fuel cell using a microchannel flow field design has been gained. It is recommended that the water imaging experiments such as neutron imaging be conducted on a fuel cell using a microchannel flow field design to completely map out the water distribution during fuel cell operation. A further study could also involve studying the different channel and land widths to determine whether a threshold value exists where flooding in the GDL becomes dominating.

References

Anderson, R., Zhang, L., Ding, Y., Blanco, M., Bi, X. & Wilkinson, D. P. 2010. A critical review of two-phase flow in gas flow channels of proton exchange membrane fuel cells. *Journal of Power Sources*. 195: p 4531-4553.

Barbir, F. 2005. *PEM Fuel Cells: Theory and Practice*. London: Elsevier Inc. p 17-201.

Bagotsky, V. S. 2009. *Fuel Cells Problems and Solutions*. New Jersey: John Wiley & Sons, Inc. p 54-57.

Basu, S. Ed. 2007. *Recent Trends in Fuel Cell Science and Technology*. New York: Springer. p 41-141

Bevers, D., Rogers, R. & von Bradke, M. 1996. Examination of the influence of PTFE coating on the properties of carbon paper in polymer electrolyte fuel cells. *Journal of Power Sources.* 63(2): p 193-201.

Busick, D. N & Wilson, M. S. 1999. Low-cost composite materials for PEFC bipolar plates. *Fuel Cells Bulletin*. 2(5): p 6-8.

Carrette, L., Friedrich, K. A. & Stimming, U. 2001. Fuel Cells - Fundamentals and Applications. *Fuel Cells.* 1(1): 5-39.

Cha, S. W., O'Hayre, R., Park, Y. & Prinz, F. B. 2006. Electrochemical impedance investigation of flooding in micro-flow channels for proton exchange membrane fuel cells. *Journal of Power Sources.* 161(1): p 138-142.

Cha, S. W., O'Hayre, R. & Prinz, F. B. 2004. The influence of size scale on the performance of fuel cells. *Solid State Ionics.* 175: p 789-795.

Cheah, M. J., Kevrekidis, I. G. & Benziger, J. B. 2013. Water Slug Formation and Motion in Gas Flow Channels: The Effects of Geometry, Surface Wettability and Gravity. *Langmuir*. 29: p 9918-9934.

Cho, S. C., Wang, Y. & Chen, K. S. 2012. Droplet dynamics in a polymer electrolyte fuel cell gas flow channel: Forces, deformation, and detachment. I: Theoretical and numerical analyses. *Journal of Power Sources.* 206: p 119-128.

Cooper, K. R., Ramani, V., Fenton, J. M. & Kunz H. R. 2005. *Experimental Methods and Data Analysis*. Scribner Associates, Inc. p. 10-48

Costamagna, P. & Srinivasan, S. 2001. Quantum jumps in the PEMFC science and technology from the 1960s to the year 2000: Part I. Fundamental scientific aspects. *Journal of Power Sources.* 102: p 242-252.

Costamagna, P. & Srinivasan, S. 2001. Quantum jumps in the PEMFC science and technology from the 1960s to the year 2000: Part II. Engineering, technology development and application aspects. *Journal of Power Sources.* 102: p 253-269.

Davey, J. R., Mukudan, R., Spendelow, J., Hussey, D. S., Jacobson, D. L., Arif, M. & Borup, R. L. 2008. Water Dynamics in a PEM Fuel Cell: Effect of Current and Humidity Transients. *ECS Transactions*. 16(2): p 329-340.

Dotelli, G., Omati, L., Stampino, P. G., Grassini, P. & Brivio, D. 2011. Investigation of gas diffusion layer compression by electrochemical impedance spectroscopy on running polymer electrolyte membrane fuel cells. *Journal of Power Sources*. 196: p 8955-8966.

EG & G Technical Services, Inc. 2004. *Fuel Cell Handbook*. 7th ed. United States of America. p 1-9.

Fabian, T., O'Hayre, R., Litster, S., Prinz, F.B. & Santiago, J.G. 2010. Active water management at the cathode of a planar air-breathing polymer electrolyte membrane fuel cell using an electroosmotic pump. *Journal of Power Sources.* 195(11): p 3640-3644.

Ge, S., Li, X., Yi, B. & Hsing, I. 2005. Absorption, Desorption, and Transport of Water in Polymer Electrolyte Membranes for Fuel Cells. *Journal of the Electrochemical Society.* 152(6): p A1149-A1157.

Gebregergis, A., Pillay, P. & Rengaswemy, R. 2008. PEMFC Fault Diagnosis, Modeling, and Mitigation. *Industry Applications Society Annual Meeting, 2008. IAS '08. IEEE.* 46(1): p 295-303.

Gerteisen, D., Heilmann, T. & Ziegler C. 2009. Modeling the phenomenon of dehydration and flooding of a polymer electrolyte membrane fuel cell. *Journal of Power Sources*. 187: p 165-181.

Gerteisen, D., Zamel, N., Sadeler, C., Geiger, F., Ludwig, V. & Hebling, C. 2012. Effect of operating conditions on current density distribution and high frequency resistance in a segmented PEM fuel cell. *International Journal of Hydrogen Energy.* 37(9): p 7736-7744.

Goebel, S.G. 2011. Impact of land width and channel span on fuel cell performance. *Journal of Power Sources.* 196(18): p 7550-7554.

Gubler, L. & Scherer, G.G. 2010. Trends for fuel cell membrane development. *Desalination.* 250(3): p 1034-1037.

Hakenjos, A., Muenter, H., Wittstadt, U. & Hebling, C. 2004. A PEM fuel cell for combined measurement of current and temperature distribution, and flow field flooding. *Journal of Power Sources.* 131: p 213-216.

He, W., Lin, G. & Nguyen, T. V. 2003. Diagnostic Tool to Detect Electrode Flooding in Proton-Exchange-Membrane Fuel Cells. *AIChE Journal*. 49(12): p 3221-3228.

Hentall, P.L., Lakeman, J.B., Mepsted, G.O., Adcock, P.L. & Moore, J.M. 1999. New materials for polymer electrolyte membrane fuel cell current collectors. *Journal of Power Sources.* 80: p 235-241.

Hermann, A., Chaudhuri, T. & Spagnol, P. 2005. Bipolar plates for PEM fuel cells: A review. *International Journal of Hydrogen Energy.* 30(12): p 1297-1302.

Hsieh, S. & Chu, K. 2007. Channel and rib geometric scale effects of flow field plates on the performance and transient thermal behavior of a micro-PEM fuel cell. *Journal of Power Sources.* 173(1): p 222-232.

Hussaini, I. S. & Wang, C. 2009. Visualization and quantification of cathode channel flooding in PEM fuel cells. *Journal of Power Sources.* 187(2): p 444-451.

Ito, K., Ashikaga, K., Masuda, H., Oshima, T., Kakimoto, Y. & Sasaki, K. 2008. Estimation of flooding in PEMFC gas diffusion layer by differential pressure measurement. *Journal of Power Sources.* 175(2): p 732-738.

Ihonen, J., Jaouen, F., Lindbergh, G. & Sundholm, G. 2001. A novel polymer electrolyte fuel cell for laboratory investigations and in-situ contact resistance measurements. *Electrochimica Acta*. 46: p 2899-2911.

Jeong, K. S. & Oh, B. S. 2002. Fuel economy and life-cycle cost analysis of a fuel cell hybrid vehicle. *Journal of Power Sources.* 105(1): p 58-65.

Jeong, S. U., Cho, E. A., Kim, H., Lim, T., Oh, I. & Kim, S. H. 2006. A study on cathode structure and water transport in air-breathing PEM fuel cells. *Journal of Power Sources.* 159(2): p 1089-1094.

Kandlikar, S. G. & Grande, W. J. 2002. Evolution of microchannel flow passages – Thermohydraulic performance and fabrication technology. *Proceedings of ASME International Mechanical Engineering Congress and Exposition.* New Orleans, Louisiana: November 17-22

Kandlikar, S. G. 2008. Microscale and Macroscale Aspects of Water Management Challenges in PEM Fuel Cells. *Heat Transfer Engineering*. 29(7): p 575-587.

Karimi, G., Jamekhorshid, A., Azimifar, Z. & Li, X. 2011. Along-channel flooding prediction of polymer electrolyte membrane fuel cells. *International Journal of Energy Research.* 35(10): p 883-896.

Karimi, S., Fraser, N., Roberts, B. & Foulkes, F. R. 2012. A review of metallic bipolar plates for proton exchange membrane fuel cells: Materials and fabrication methods. *Advances in Materials Science and Engineering.*: p 1-22.

Kim, S., Shimpalee, S. & Van Zee, J. W. 2004. The effect of stoichiometry on dynamic behavior of a proton exchange membrane fuel cell (PEMFC) during load change. *Journal of Power Sources*. 135: p 110-121.

Koç, M. & Mahabunphachai, S. 2007. Feasibility investigations on a novel micro-manufacturing process for fabrication of fuel cell bipolar plates: Internal pressure-assisted embossing of micro-channels with in-die mechanical bonding. *Journal of Power Sources*. 172: p 725-733.

Kulikovsky, A.A. 2004. The effect of stoichiometric ratio λ on the performance of a polymer electrolyte fuel cell. *Electrochimica Acta.* 49(4): p 617-625.

Kumar, A. & Reddy, R. G. 2003. Effect of channel dimensions and shape in the flow-field distributor on the performance of polymer electrolyte membrane fuel cells. *Journal of Power Sources.* 113(1): p 11-18.

Kumbur, E.C., Sharp, K.V. & Mench, M.M. 2006. Liquid droplet behavior and instability in a polymer electrolyte fuel cell flow channel. *Journal of Power Sources.* 161(1): p 333-345.

Larminie, J. & Dicks, A. 2003. *Fuel Cell Systems Explained*. 2nd ed. England: John Wiley & Son Ltd. p 67-110.

Le Canut, J. M., Latham, R., Merida, W. & Harrington, D. A. 2009. Impedance study of membrane dehydration and compression in proton exchange membrane fuel cells. *Journal of Power Sources.* 192: p 457-466.

Lee, W., Ho, C., Van Zee, J. W. & Murthy, M. 1999. The effects of compression and gas diffusion layers on the performance of a PEM fuel cell. *Journal of Power Sources*. 84(1): p 45-51.

Lee, S. J., Chang-Chien, A., Cha, S. W., O'Hayre, R., Park, Y. I., Saito, Y. & Prinz, F. B. 2002. Design and fabrication of a micro fuel cell array with "flip-flop" interconnection. *Journal of Power Sources.* 112(2): p 410-418.

Lee, S. J., Hsu, C. D. & Huang, C. H. 2005. Analyses of the fuel cell stack assembly pressure. *Journal of Power Sources*. 145: p 353-361.

Lee, M., Chen, T. H., Lee, W. S., Lin, B. S., Lau, B. Y., Tsai, P. F. & Wang, G. C. 2011. From microstructure to the development of water and major reaction sites inside the catalyst layer of the cathode of a proton exchange membrane fuel cell. *Journal of Power Sources.* 196(18): p 7411-7419.

Li, H., Tang, Y., Wang, Z., Shi, Z., Wu, S., Song, D., Zhang, J., Fatih, K., Zhang, J., Wang, H., Liu, Z., Abouatallah, R & Mazza, A. 2008. A review of water flooding issues in the proton exchange membrane fuel cell. *Journal of Power Sources.* 178(1): p 103-117.

Li, X. & Sabir, I. 2005. Review of bipolar plates in PEM fuel cells: Flow-field designs. *International Journal of Hydrogen Energy.* 30(4): p 359-371.

Li, X., Sabir, I. & Park, J. 2007. A flow channel design procedure for PEM fuel cells with effective water removal. *Journal of Power Sources.* 163(2): p 933-942.

Lin, G. & Nguyen, T. V. 2005. Effect of Thickness and Hydrophobic Polymer Content of the Gas Diffusion Layer on Electrode Flooding Level in a PEMFC. *Journal of the Electrochemical Society.* 152(10): p A1942-A1948.

Lin, G. & Nguyen, T. V. 2006. A Two-Dimensional Two-Phase Model of a PEM Fuel Cell. *Journal of the Electrochemical Society.* 153(2): p A372-A382.

Ma, H. P., Zhang, H. M., Hu, J., Cai, Y. H. & Yi, B. L. 2006. Diagnostic tool to detect liquid water removal in the cathode channels of proton exchange membrane fuel cells. *Journal of Power Sources.* 162(1): p 469-473.

McCrabb, H., Taylor, E. J., Lozano-Morales, A., Shimpalee, S., Inman, M. & Van Zee J. W. 2010. Through-mask Electro-etching for Fabrication of Metallic Bipolar Plate gas Flow Field Channels. *ECS Transactions*. 33(1): p 991-1006.

Mahabunphachai, S. & Koç, M. 2008. Fabrication of micro-channel arrays on thin metallic sheet using internal fluid pressure: Investigation on size effects and development of design guidelines. *Journal of Power Sources*. 175: p 363-371.

Manso, A. P., Marzo, F. F., Barranco, J., Garikano, X. & Mujika, M. G. 2012. Influence of geometric parameters of flow fields on the performance of a PEM fuel cell. A review. *International Journal of Hydrogen Energy*. 37: p 15256-15287.

Marcinkoski, J., Kopasz, J. P. & Benjamin, T. G. 2008. Progress in the US DOE fuel cell subprogram efforts in polymer electrolyte fuel cells. *International Journal of Hydrogen Energy.* 33(14): p 3894-3902.

Mason, T. J., Millichamp, J., Neville, T. P., El-kharouf, A., Pollet, B. G. & Brett, D. J. L. 2012. Effect of clamping pressure on ohmic resistance and compression of gas diffusion layers for polymer electrolyte fuel cells. *Journal of Power Sources*. 219: p 52-59.

Nam, J. H., Lee, K., Sohn, S. & Kim, C. 2009. Multi-pass serpentine flow-fields to enhance under-rib convection in polymer electrolyte membrane fuel cells: Design and geometrical characterization. *Journal of Power Sources.* 188(1): p 14-23.

Nguyen, T. V. 1996. A Gas Distributor Design for Proton-Exchange-Membrane Fuel Cells. *Journal of the Electrochemical Society.* 143(5): p L103-L105.

Nguyen, T. V. 2006. Water Management by Material Design and Engineering for PEM Fuel Cells. *ECS Transactions*. 3(1): p 1171-1180.

Opu, M. S., Choi, D., Ohashi, M., Shimpalee, S. & Van Zee, J. W. 2010. Understanding Differences in the Performance of Laboratory Scale PEMFCs: I. The Effect of Active-Area. *ECS Transactions.* 33(1): p 1017-1025.

Owejan, J. P., Trabold, T. A., Jacobson, D. L., Arif, M. & Kandlikar, S. G. 2007. Effects of flow field and diffusion layer properties on water accumulation in a PEM fuel cell. *International Journal of Hydrogen Energy.* 32(17): p 4489-4502.

Park, G., Sohn, Y., Yang, T., Yoon, Y., Lee, W. & Kim, C. 2004. Effect of PTFE contents in the gas diffusion media on the performance of PEMFC. *Journal of Power Sources.* 131: p 182-187.

Pasaogullari, U. & Wang, C. 2004. Two-phase transport and the role of micro-porous layer in polymer electrolyte fuel cells. *Electrochimica Acta.* 49(25): p 4359-4369.

Pasaogullari, U., Wang, C. & Chen, K. S. 2005. Two-Phase Transport in Polymer Electrolyte Fuel Cells with Bilayer Cathode Gas Diffusion Media. *Journal of the Electrochemical Society.* 152(8): p A1574-A1582.

Pearsall, J. Ed. 1999. *The Concise Oxford Dictionary*. 10th ed. New York: Oxford University Press Inc.: p 137.

Qi, Z. & Kaufman, A. 2002. Improvement of water management by a microporous sublayer for PEM fuel cells. *Journal of Power Sources.* 109(1): p 38-46.

Quan, P. & Lai, M. C. 2007. Numerical study of water management in air flow channel of PEM fuel cell cathode. *Journal of Power Sources*. 164(1): p 222-237.

Rayment, C. & Sherwin, S. 2003. *Introduction to Fuel Cell Technology*. University of Notre Dame, United States of America. p 99.

Schmittinger, W. & Vahidi, A. 2008. A review of the main parameters influencing long term performance and durability of PEM fuel cells. *Journal of Power Sources*. 180: p 1-14.

Serway, R. A. & Jewett, J. W. 2014. *Physics for Scientists and Engineers with modern physics*. United States of America: Brooks/Cole. p. 746-814.

Shimpalee, S., Greenway, S. & Van Zee, J. W. 2006. The impact of channel path length on PEMFC flow-field design. *Journal of Power Sources.* 160(1): p 398-406.

Shimpalee, S., Lilavivat, V., Van Zee, J. W., McCrabb, H. & Lozano-Morales, A. 2011. Understanding the effect of channel tolerances on performance of PEMFCs. *International Journal of Hydrogen Energy*. 36: p 12512-12523.

Siefert, N. S. & Litster, S. 2011. Voltage loss and fluctuation in proton exchange membrane fuel cells: The role of cathode channel plurality and air stoichiometric ratio. *Journal of Power Sources.* 196(4): p 1948-1954.

Spernjak, D., Prasad, A. K. & Advani, S. G. 2007. Experimental investigation of liquid water formation and transport in a transparent single-serpentine PEM fuel cell. *Journal of Power Sources.* 170(2): p 334-344.

Spiegel, C. S., Agarwal, R. & Bhansali, S. 2008. Comparison of microchannel dimensions for air-breathing polymer exchange membrane microfuel cells. *Journal of Power Sources.* 182(2): p 603-608.

Spiegel, C. 2008. *PEM Fuel Cell Modelling and Simulation Using Matlab.* London Elsevier Inc. p 269-359

Taherian, R. 2014. A review of composite and metallic bipolar plates in proton exchange membrane fuel cell: Materials, fabrication, and material selection. *Journal of Power Sources.* 265: p 370-390.

Tsuchiya, H. & Kobayashi, O. 2004. Mass production cost of PEM fuel cell by learning curve. *International Journal of Hydrogen Energy.* 29(10): p 985-990.

Tüber, K., Pócza, D. & Hebling, C. 2003. Visualization of water buildup in the cathode of a transparent PEM fuel cell. *Journal of Power Sources.* 124(2): p 403-414.

Turhan, A., Heller, K., Brenizer, J. S. & Mench, M. M. 2006. Quantification of liquid water accumulation and distribution in a polymer electrolyte fuel cell using neutron imaging. *Journal of Power Sources.* 160(2): p 1195-1203.

Ueki, T. & Watanabe, M. 2008. Macromolecules in Ionic Liquids: Progress, Challenges and Opportunities. *Macromolecules*. 41(11): p 3739-3749

US Department of Energy. 2011. *The Department of Energy Hydrogen and Fuel Cells Program Plan: An Integrated Strategic Plan for the Research, Development, and Demonstration of Hydrogen and Fuel Cells Technologies.* Washington: p 8-42.

Vielstich, W., Gasteiger, H, A. & Lamm, A. Eds. 2003. *Handbook of Fuel Cells – Fundamentals, Technology and Applications. Volume 1: Fundamentals and Survey of Systems.* John Wiley & Sons, Ltd.: p 49926-49929.

Wang, J. & Wang, H. 2012. Flow-Field Designs of Bipolar Plates in PEM Fuel Cells: Theory and Applications. *Fuel Cells.* 12(6): p 989-1003.

Wang, X., Zhang, X., Yan, W., Lee, D. & Su, A. 2009. Determination of the optimal active area for proton exchange membrane fuel cells with parallel, interdigitated or serpentine designs. *International Journal of Hydrogen Energy.* 34(9): p 3823-3832.

Wang, Y., Wang, C. & Chen, K. S. 2007. Elucidating differences between carbon paper and carbon cloth in polymer electrolyte fuel cells. *Electrochimica Acta.* 52(12): p 3965-3975.

Weber, A. Z. & Newman, J. 2005. Effects of Microporous Layers in Polymer Electrolyte Fuel Cells. *Journal of the Electrochemical Society.* 152(4): A677-A688.

Wilkinson, D. P., Voss, H. H. & Prater, K. 1994. Water management and stack design for solid polymer fuel cells. *Journal of Power Sources.* 49(1–3): p 117-127.

Williams, M. V., Kunz, H. R. & Fenton, J. M. 2004. Influence of Convection Through Gas-Diffusion Layers on Limiting Current in PEM FCs Using a Serpentine Flow Field. *Journal of the Electrochemical Society.* 151(10): p A1617-A1627.

Wind, J., Späh, R., Kaiser, W. & Böhm, G. 2002. Metallic bipolar plates for PEM fuel cells. *Journal of Power Sources.* 105(2): p 256-260.

Wu, J., Yuan, X. Z., Wang, H., Blanco, M., Martin, J. J. & Zhang, J. 2008. Diagnostic tools in PEM fuel cell research: Part I: Electrochemical techniques. *International Journal of Hydrogen Energy.* 33(6): p 1735-1746.

Xu, C. & Zhao, T. S. 2007. A new flow field design for polymer electrolyte-based fuel cells. *Electrochemistry Communications*. 9: p 497-503.

Yamada, H., Hatanaka, T., Murata, H. & Morimoto, Y. 2006. Measurement of Flooding in Gas Diffusion Layers of Polymer Electrolyte Fuel Cells with Conventional Flow Field. *Journal of the Electrochemical Society.* 153(9): p A1748-A1754.

Yan, W., Wang, X., Mei, S., Peng, X., Guo, Y. & Su, A. 2008. Effects of operating temperatures on performance and pressure drops for a 256 cm2 proton exchange membrane fuel cell: An experimental study. *Journal of Power Sources.* 185(2): p 1040-1048.

Yao, S. & Santiago, J. G. 2003. Porous glass electroosmotic pumps: theory. *Journal of Colloid and Interface Science.* 268(1): p 133-142.

Yi, J. S., Yang, D. & King, C. 2004. Water Management along the Flow Channels of PEM Fuel Cells. *AIChE Journal*. 50(10): p 2594-2603.

Yousfi-Steiner, N., Moçotéguy, P., Candusso, D.,Hissel, D., Hernandez, A. & Aslanides, A. 2008. A review on PEM voltage degradation associated with water management: Impacts, influent factors and characterization. *Journal of Power Sources*. 183: p 260-274.

Yuan, X. Z., Song, C., Wang, H. & Zhang, J. 2010. *Electrochemical Impedance Spectroscopy in PEM Fuel Cells*. London Springer. p. 26-191.

Yuan, X., Wang, H., Colin Sun, J. & Zhang, J. 2007. AC impedance technique in PEM fuel cell diagnosis—A review. *International Journal of Hydrogen Energy.* 32(17): p 4365-4380.

Zhang, J., Li, H., Shi, Z. & Zhang, J. 2010. Effects of Hardware Design and Operation Conditions on PEM Fuel Cell Water Flooding. *International Journal of Green Energy.* 7(5): p 461-474.

Zhang, J., Li, H. & Zhang, J. 2009. Effect of Operating Backpressure on PEM Fuel Cell Performance. *ECS Transactions.* 19(31): p 65-76.

Zhou, P., Wu, C. W. & Ma, G. J. 2007. Influence of clamping force on performance of PEMFCs. *Journal of Power Sources*. 163: p 874-881.

Zoulias, E., Varkaraki, E., Lymberopoulos, N., Christodoulos, C. N. & Karagiorgis, G. N. 2004. A Review On Water Electrolysis. *TCJST*. 4(2): p 41-71.

Appendix

Summary of Fuel Cell Tests and Operating Conditions

Test #	Flow field	Torque / Nm	Operating conditions					Diagnostic tests
			T / °C	P / bar	RH / %	S_{anode}	$S_{cathode}$	
1	Microchannel	1	80	1	100%	1.5 @ 1.5 A cm^{-2}	2, 2.5, 3 & 4 @ 1.5 A cm^{-2}	• Polarization curves • High frequency resistance • Electrochemical impedance spectroscopy at 0.25 and 1.2 A cm^{-2}
2	Microchannel	1.6						
3	Microchannel	2.6						
4	Commercial	1						
5	Commercial	1.6						
6	Commercial	2.6						
7	Microchannel	1.6				1.5	2, 2.5, 3 & 4	• Pressure drop co-efficient measurements • Cell voltage monitoring
8	Commercial	1.6						
9	Microchannel	1.6		Anode - 1 Cathode- Varying*		1.5	2	• Polarization curves • High frequency resistance

NB. T = temperature, P = Pressure, RH = Relative Humidity of anode and cathode, S_{anode} = stoichiometry of anode, $S_{cathode}$ = stoichiometry of cathode.
*described in table below

Stoichiometric Ratio	Oxygen Partial Pressure (bar)	Required operating pressure at stoichiometric ratio of 2 (bar)
2.0	0.108	1.00
4.0	0.148	1.18

Oxygen Partial Pressure versus Drag Force Calculation

The average oxygen partial pressures in the PEFC corresponding to air stoichiometric ratios of 2 and 4 were calculated from the inlet and exit oxygen partial pressures at the different stoichiometries. The required air flow rates at the different stoichiometries were based on a current density of 1.5 Acm^{-2}. The inlet oxygen partial pressure was deduced from the mole fractions of water vapour and synthetic air fed at the different air stoichiometric ratios. The mole fraction of oxygen in the synthetic air was provided by the supplier, Air Products. The Antoine Equation was used to determine the mole fraction of water vapour in cathode feed. Because the synthetic air was saturated with water vapour and the operation temperature was fixed, the amount of water vapour throughout the PEFC was constant for the different air stoichiometric ratios.

The exit oxygen partial pressures was determined by subtracting the amount of oxygen consumed during the oxygen reduction reaction from the amount of oxygen fed at the different air stoichiometric ratios. The amount of water vapour and nitrogen in the inlet was the same as in the outlet because they did not participate in the overall oxygen reduction reaction. The partial pressure of oxygen in the outlet was then determined as the mole fraction of oxygen in the water vapour, nitrogen and oxygen PEFC exit mixture.

Besides changing the stoichiometric ratios, the operation pressure can be changed to vary the average oxygen partial pressure in the PEFC. The stoichiometric ratio can remain fixed while the operation pressure is increased to obtain the same change in average oxygen partial pressure obtained from increasing the air stoichiometric ratios at a fixed operation pressure. To achieve the same change in average oxygen partial pressure using the two different methods, the pressure drop between the PEFC's inlet and outlet must also remain fixed in both methods.

Calculation of Hydrogen inlet volumetric flow rate

The number of moles of hydrogen, n_{H2}, consumed at a current density of 1.5 Acm^{-2} is given by;

$$n_{H2} = I * Active\ Area * \frac{1}{\#F}$$

$$= 1.5 * 25 * \frac{1}{2 * 96490}$$

$$\approx 1.943 * 10^{-4}\ mol/s$$

Therefore the number of moles that correspond to a stoichiometric ratio of 1.5 are;

$$\approx 1.5 * 1.943 * 10^{-4}$$

$$\approx 2.915 * 10^{-4}\ mol/s$$

The volumetric flow of hydrogen, V_{H2}, fed to the PEFC is obtained from the ideal gas equation. The temperature and pressure used are governed by that calibrated for the hydrogen inlet value (273.15 K and 1 Bara).

$$V_{H2} = \frac{n_{H2} * RT}{P}$$

$$= \frac{2.915 * 10^{-4} * 8.314 * 273.15}{101325}$$

$$\approx 6.533 * 10^{-6}\ \frac{m^3}{s}$$

$$\approx 0.40\ litres\ per\ min$$

Calculation of Air inlet volumetric flow rate

The number of moles of oxygen, n_{O2}, consumed by the oxygen reduction reaction is given by;

$$n_{O2} = I * Active\ Area * \frac{1}{2\#F}$$

$$= 1.5 * 25 * \frac{1}{4 * 96490}$$

$$\approx 9.716 * 10^{-5}\ mol/s$$

Therefore the number of moles that correspond to a stoichiometric ratio of 2 are;

$$\approx 2 * 9.716 * 10^{-5}$$

$$\approx 1.943 * 10^{-5}\ mol/s$$

The total moles of air, n_{air}, that must be fed to the PEFC are given by;

$$n_{air} = \frac{n_{O2}}{0.21}$$

$$\approx \frac{1.943 * 10^{-5}}{0.21}$$

$$\approx 9.253 * 10^{-4}\ mol/s$$

The volumetric flow of air, V_{air}, fed to the PEFC is obtained from the ideal gas equation. The temperature and pressure used are governed by that calibrated for the air inlet value (273.15 K and 1 Bara).

$$V_{air} = \frac{n_{air} * RT}{P}$$

$$= \frac{9.253 * 10^{-4} * 8.314 * 273.15}{101325}$$

$$\approx 2.074 * 10^{-5}\ \frac{m^3}{s}$$

$$\approx 1.25\ litres\ per\ min$$
